particles

MDPI

Article

A Study of the Properties of the QCD Phase Diagram in High-Energy Nuclear Collisions

Xiaofeng Luo [1,†], Shusu Shi [1,*,†], Nu Xu [1,2,†] and Yifei Zhang [3,†]

[1] Key Laboratory of Quark & Lepton Physics (MOE) and Institute of Particle Physics, Central China Normal University, Wuhan 430079, China; xfluo@mail.ccnu.edu.cn (X.L.); nxu@lbl.gov (N.X.)
[2] Institute of Modern Physics, Chinese Academy of Sciences, Lanzhou 730000, China
[3] State Key Laboratory of Particle Detection and Electronics, University of Science and Technology of China, Hefei 230026, China; ephy@ustc.edu.cn
* Correspondence: shiss@mail.ccnu.edu.cn
† The authors contribute equally to this paper.

Received: 28 February 2020; Accepted: 24 March 2020; Published: 1 April 2020

Abstract: With the aim of understanding the phase structure of nuclear matter created in high-energy nuclear collisions at finite baryon density, a beam energy scan program has been carried out at Relativistic Heavy Ion Collider (RHIC). In this mini-review, most recent experimental results on collectivity, criticality and heavy flavor productions will be discussed. The goal here is to establish the connection between current available data and future heavy-ion collision experiments in a high baryon density region.

Keywords: baryon density; collectivity; criticality; hadron gas; heavy flavor; QCD phase diagram; Quark-gluon-plasma (QGP)

1. Introduction

Most of the visible matter in our universe can be described by the Quantum Chromdynamics (QCD), the standard theory of strong interactions. In the beginning of the century, the new form of matter, the quark-gluon plasma (QGP) in which quarks and gluons are 'freed' in a much larger volume compared to that of nucleon's, was discovered in the largest heavy-ion colliders RHIC and LHC [1–4] at vanishing baryonic density. Soon after the discovery, a serious question was asked: what is the structure of the nuclear matter at high baryonic density?

Tremendous efforts from both experimental and theoretical sides have launched in order to address the question. Figure 1 summarizes the current status of the studies. At the zero baryonic density, the transition from QGP to hadronic matter is a smooth-crossover at $T = 150 - 160$ MeV [5–9], see dashed-line in the figure. These results are extracted from the state of the art Lattice gauge theory calculations. At high baryonic density, on the other hand, one would expect a first-order phase transition, shown as a black solid-line. Thermodynamically the first-order phase boundary line must end at finite baryonic density, this is the illusive QCD critical point (CP). Again, recent Lattice calculations have concluded that the QCD critical is 'unfavored' [10,11] when $\mu_B/T < 2.5$. The red-line is the chemical freeze-out curve extracted from the measured hadron yields. The collision energies with the corresponding accelerator complex are indicated at the top of the figure.

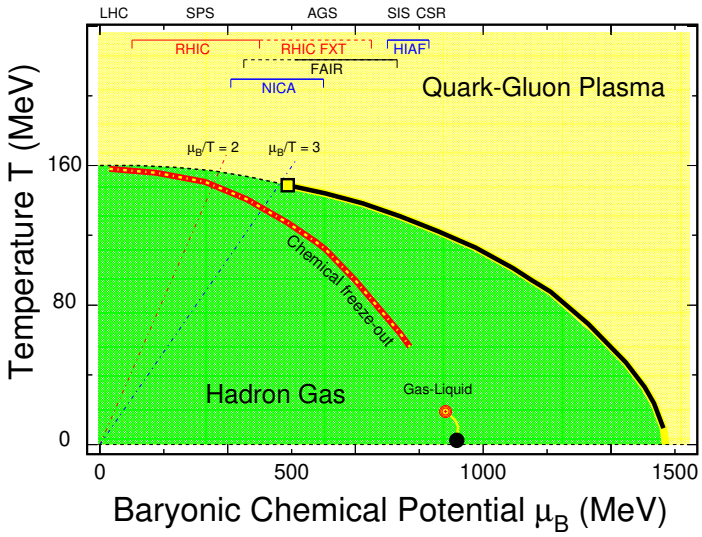

Figure 1. (Color online) Schematic Quantum Chromdynamics (QCD) phase diagram in the thermodynamic parameter space spanned by the temperature T and baryonic-chemical potential μ_B. Experimentally extracted chemical freeze-out parameters are shown as the red-line [12]. The dashed-line near $\mu_B = 0$ indicates the crossover transition from the Quark-Gluon-Plasma to Hadron Gas [5–9]. The solid-line and the square show the expected 1st-order phase boundary and its end point: critical point. The regions of $\mu_B/T < 2$ and < 3 are shown as red and blue dot-dashed lines, respectively. The Lattice QCD calculations have concluded that the QCD critical point is unlikely to exist at $\mu_B/T < 2.5$ [10,11]. The red-circle and the yellow-line represent the liquid-gas transition [13]. Regions for physics programs of RHIC beam energy scan and fixed-target (US) [14], NICA (Russia) [15], FAIR (Germany) [16] as well as the HIAF (China) [17] are indicated at the top of the plot.

Experimental status on the beam energy scan (BES) is highlighted in Figure 2. Plot (a) shows the chemical freeze-out temperature $T_{\rm ch}$ as a function of the baryonic chemical potential μ_B. Both ALICE at LHC and STAR at RHIC results clearly show that at the vanishing baryon density, i.e., at high collision energy, the data driven freeze-out temperature is consistent with the Lattice calculation, $T_{ch} \sim 160$ MeV. Many authors have tried to analyze the chemical freeze-out conditions. Those include the results fluctuations analysis from Lattice QCD [18–22], HRG model [12] and other methods [23,24]. In the low baryon density region, $\mu_B \leq 400$ MeV, the μ_B dependence of the freeze-out temperature is quite weak and the value of the freeze-out temperature is around 150–160 MeV. More dramatic drop of the temperature is seen in the high baryon density region. Plot (b) is the kaon over pion yield ratios, extracted from central heavy-ion collisions, as a function of the collision energies. While one observes the smooth increase of the negative kaon over pion ratio with the collision energy, the positive ratio shows a broad peak around $\sqrt{s_{NN}} \sim 8$ GeV and eventually merged with the negative ratios at high collision energy, $\sqrt{s_{NN}} \geq 100$ GeV, where the pair production becomes dominant. Due to the associate channel, $N + N \rightarrow N + \Lambda + K^+$, positive kaons carry information on baryon density. The peak in plot (b) implies the maximum freeze-out density reached at 8 GeV. Later in the discussions, we attribute the region of $2 \leq \sqrt{s_{NN}} \leq 8$ GeV as the high baryon density region (HBDR) as indicated by the yellow-area in the plot.

Collective flow (collectivity) and the critical behavior (criticality) are important aspects in high-energy nuclear collisions. In this short review, we will discuss the experimental status including the results on collectivity and criticality from high-energy nuclear collisions. RHIC has provided most recent data so we will focus on the information. At the end we will address the importance of the future fixed-target experiments such as STAR fixed-target program in BES-II, CBM at FAIR [16] as well the CEE at HIAF [17].

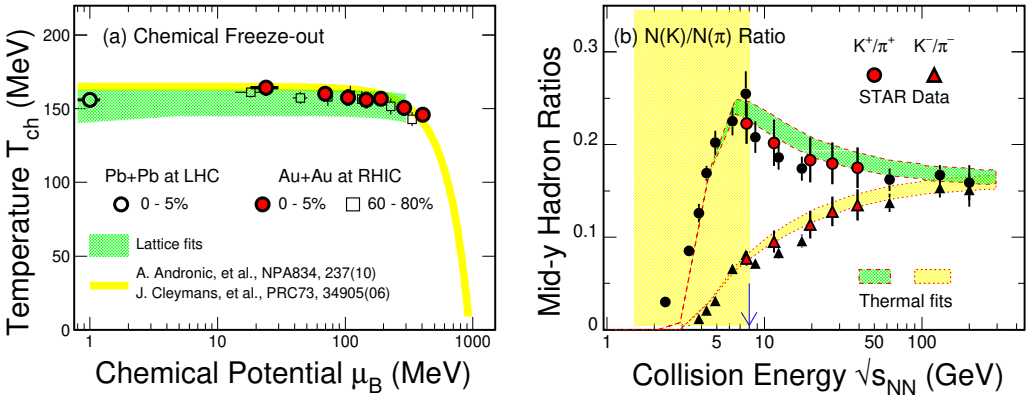

Figure 2. (Color online) (**a**) Experimental results of chemical freeze-out temperature as a function of the baryonic chemical potential from the RHIC BES-I [12] and LHC [25,26]. Red-circles and black-squares represent results from the top 5% and 60–80% Au+Au collisions at RHIC, respectively. Open-circle is from the 2.76 TeV 0–5% Pb+Pb collisions at LHC. The hatched green-band represents the Lattice results [7,27]. The yellow-line shows the empirical thermal fits results [28,29]. (**b**) Mid-rapidity particles of positive and negative kaons over pions shown as circles and triangles, respectively. The results [30] of thermal model fits are shown as hatched-bands in the plot and the high-baryon-density region is highlighted in yellow.

2. Beam Energy Dependence of the Collectivity

The main goal of high energy heavy-ion collisions, such as collisions at LHC and top energy collisions at RHIC, is to study the properties of new form of matter QGP. QGP is a thermalized (or nearly) system with partonic degree of freedom. The elliptic flow measurement of multi-strange hadrons and ϕ mesons indicates the partonic collectivity has been built up at the top energy heavy-ion collisions at RHIC [31–37]. The Heavy Flavor Tracker, a high resolution silicon detector system, which was installed in the year of 2013, provides high vertex position resolution. The significance of charmed hadron reconstruction is significantly improved. Thus the precise measurement of D^0 becomes possible. Figure 3 shows the v_2 results for D^0, Ξ^-, Λ and K^0_S [38]. A number of constituent quark (n_q) is tested by scaling both v_2 and $m_T - m_0$ with n_q. A simple quark coalescence or recombination model suggests the baryon v_2 would be 1.5 times of the meson v_2 assuming the collectivity has been attained in the partonic stage, as the number of constituent quarks for baryons is 3 where it is 2 for mesons. When discussing the n_q scaling, we usually focus on the intermediate p_T range in which the v_2 value saturates. The D^0 v_2 follows the n_q scalings with selected multi-strange and strange hadrons in Figure 3. It indicates the collectivity of parton level has been built up from light flavor u, d quarks to strange and charm quarks. Since the mass of the charm-quark is much larger than the temperature reached in the system, the observed strong charm-quark collectivity can be interpreted as the thermalization of the medium created in the 200 GeV Au+Au collisions at RHIC [38]. To some extent, this result justified the phase diagram sketched in Figure 1.

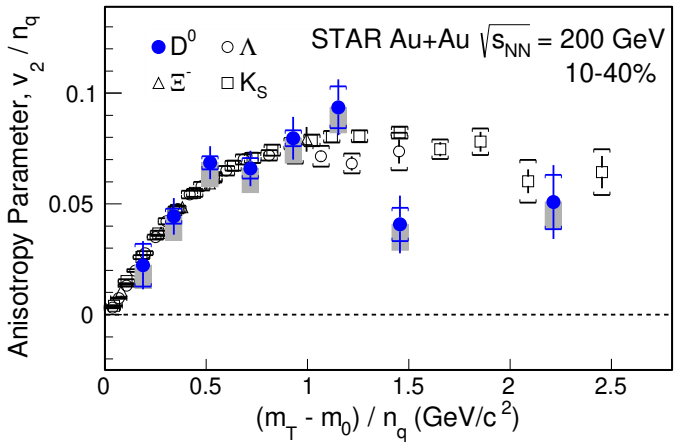

Figure 3. (Color online) The number of constituent quark (n_q) scaled v_2 as a function of $(m_T - m_0)/n_q$ in 10%–40% Au+Au collisions for D^0, Ξ^-, Λ and K^0_S (from [38]). Where m_T is square root of the rest mass squared plus transverse momentum squared.

The main motivation of BES program is to explore the QCD phase boundary and critical point. The logic is straightforward: as the collision energy decreases, the conditions of QGP formation are no longer satisfied at some point. It offers us a unique experimental way to investigate the QCD phase structure. The transverse radial flow velocity β is obtained by fitting the transverse momentum p_T spectra with a blast wave model [39]:

$$\frac{dN}{p_T dp_T} \propto \int_0^R r\, dr\, m_T\, I_0\left(\frac{p_T \sinh\rho(r)}{T_{\rm kin}}\right) \times K_1\left(\frac{m_T \cosh\rho(r)}{T_{\rm kin}}\right) \quad (1)$$

where I_0 and K_1 are the modified Bessel functions and $\rho(r) = \tanh^{-1}\beta$. The model assumes a radially boosted thermalized source with two key parameters, kinetic freeze-out temperature $T_{\rm kin}$ and a transverse collective flow velocity β.

Plot (a) of Figure 4 shows the extracted parameter β as a function of collision energy. The data points are taken from E802 [40–43], E866 [44,45], E877 [46], E895 [47], NA49 [48–51], STAR [12,52,53] and ALICE experiments [54] and references therein. The p_T spectra of $\pi^{\pm}$, $K^{\pm}$, p and $\bar{p}$ are fitted simultaneously with the blast wave model. The p_T range for simultaneous fitting are similar across all RHIC BES and LHC energies. A rapid increase of $\langle\beta\rangle$ is observed at low energies (<5 GeV), then a steady increase follows up to LHC energy. The six points from RHIC BES (7.7–39 GeV) are almost flat within uncertainties.

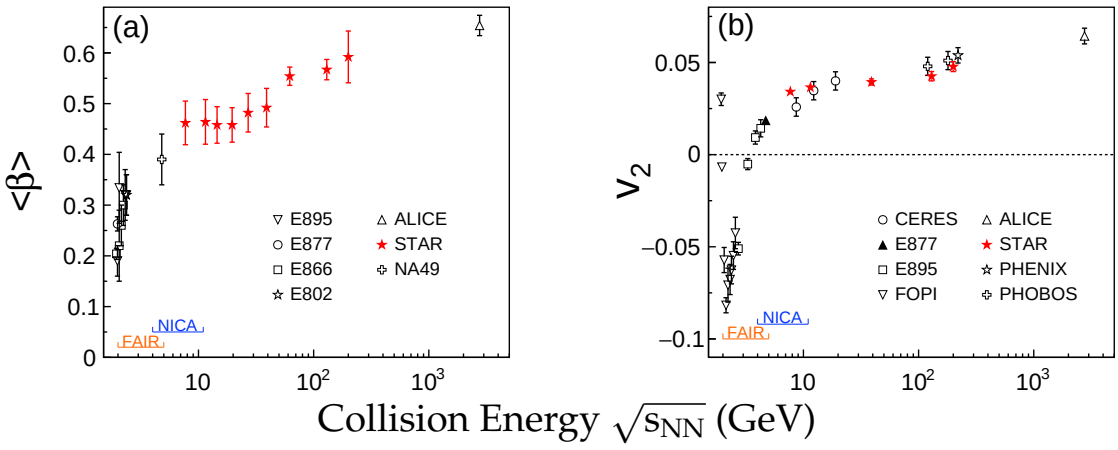

Figure 4. (Color online) (**a**) The transverse radial flow velocity as a function of collision energy from

central heavy-ion collisions. The data points are taken from E802 [40–43], E866 [44,45], E877 [46], E895 [47], NA49 [48–51], STAR [12,52,53] and ALICE experiments [54] and references therein. The data points of RHIC and LHC are from 0–5% central collisions. AGS and SPS energies are mostly from 0–5% and 0–7% central collisions respectively. (**b**) The p_T-integrated v_2 in 20%–30% most central collisions (or similar centrality) from various collision energies. The data points are from E895 [55] for protons, NA49 [56] for pions and FOPI [57], E877 [58], CERES [59], STAR and ALICE [60] for charged hadrons. The RHIC results of inclusive charged particles for 130 and 200 GeV are from refs. [61–65]. The RHIC BES data are from refs. [66,67]. The energy regions of future collider and fix-target experiments, NICA and FAIR, are indicated in both plots.

The $\langle\beta\rangle$ parameter extracted from blast wave model reflects the transverse radial flow built-up in the collision system. The second order coefficient of final azimuth distribution in the momentum space, v_2, is sensitive to the initial geometry and interactions of early stage of the collisions. It suggests that a non-monotonic variation could be observed around the so-called, "softest point of EOS" [68,69]. The "softest point of EOS" is usually defined as a strong drop of speed of sound (a minimum value) or a reduction in the pressure of the system during the dynamic evolution. Plot (b) of Figure 4 shows the p_T-integrated v_2 from 20%–30% or similar centrality as a function of collision energy. The data points are from E895 [55] for protons, NA49 [56] for pions and FOPI [57], E877 [58], CERES [59], STAR and ALICE [60] for charged hadrons. The RHIC results of inclusive charged particles for 130 and 200 GeV are from refs. [61–65]. The RHIC BES data are from refs. [66,67]. The negative v_2 ($\sqrt{s_{NN}}$ <3 GeV) is known due to the "squeeze-out" effect [57]. An increasing trend is observed for p_T integrated v_2 from AGS to LHC. It appears that the slope of v_2 with collision energy is steeper for 3–7.7 GeV compared to 7.7–2760 GeV, which is consistent with that we observe for $\langle\beta\rangle$ parameter. The v_2 of charged hadrons as a function of p_T does not change significantly at RHIC BES and LHC energies. Due to the rise in mean p_T which is expected from larger radial flow, the p_T-integrated v_2 increases. It is consistent with the collision energy dependence of $\langle\beta\rangle$ parameter, as discussed in panel (a) of Figure 4. Non-monotonic behavior which is predicted by the softening of the equation of state for a system close to the critical temperature [68] is not observed.

The first order coefficient of final azimuth distribution in the momentum space, v_1 (rapidity-odd), as a function of rapidity is sensitive to the system expansion during the early stage of collisions. Both hydrodynamic and nuclear transport models indicate that v_1 in the midrapidity region offers sensitivity to details of the expansion of the participant matter during the early collision stages [70–72]. Hydrodynamic plus first-order phase transition calculations suggest a minimum of net-baryon v_1 slope (dv_1/dy) near mid-rapidity is a signal of phase transition between QGP and hadronic matter [73,74]. Net-particle is defined as the excess yield of a particle type over its anti-particle [75,76]. The v_1 of net-particle is defined as: $v_{1X} = r(y)v_{1\bar{X}} + [1 - r(y)]v_{1\mathrm{net-X}}$, where X represents particle, $\bar{X}$ represents the corresponding anti-particle, $r(y)$ is the ratio of particle to anti-particle yield. Plot (a) of Figure 5 shows the v_1 slope relative to rapidity for net-proton, net-Λ and net-kaon. Similar energy dependence is observed for net-proton and net-Λ. The non-monotonic behavior is consistent with the hydrodynamical calculations with first-order phase transition [73,74]. Large divergence between dv_1/dy of net-kaon and net-proton (net-Λ) is observed below $\sqrt{s_{NN}} < 20$ GeV, whereas all three agrees well at and above 20 GeV. More theoretical inputs are needed to understand the difference. At the same time the measurements of centrality dependence in the future BES program will further verify the energy dependence and constrain model calculations. In Ref. [76], the dv_1/dy of ϕ mesons shows larger magnitude than pions and kaons at and above 14.5 GeV, and more interesting, the ϕ meson slope seems to increase sharply at 11.5 GeV. Because of the large statistical uncertainties, it is still not conclusive. It opens a new direction for both experimental and theoretical investigation on directed flow [77].

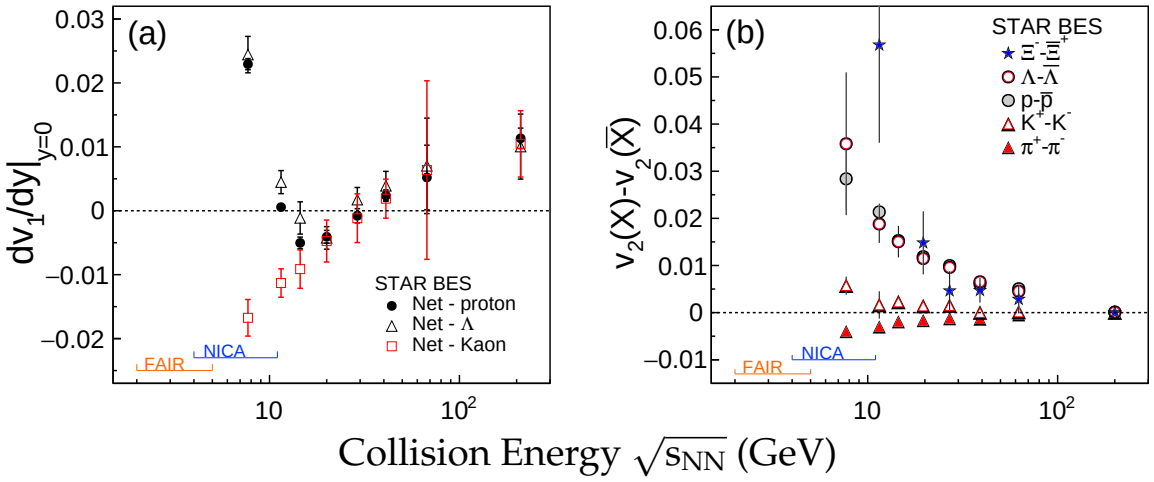

Figure 5. (Color online) (**a**) The slope of v_1 at mid-rapidity (dv_1/dy) as a function of collision energy in 10%–40% Au+Au collisions for net-proton, net-Λ and net-kaon [75,76]. (**b**)The v_2 difference between particles and the corresponding anti-particles as a function of collision energy [78–80]. The energy regions of future collider and fix-target experiments, NICA and FAIR, are indicated in both plots.

As discussed above, the v_2 of multi-strange hadrons and ϕ mesons are more sensitive to the parton level collectivity as their hadronic cross sections are smaller than light flavor hadrons [81–83]. The results from RHIC BES I suggest a possible drop of ϕ meson v_2 compared to other hadrons in Au+Au collisions at $\sqrt{s_{NN}}$ = 11.5 and 7.7 with $\sim 2\sigma$ effect [78–80]. Data of high precision will be available with RHIC BES II. A significant difference in the v_2 values between particles and the corresponding anti-particles is observed at low energy heavy-ion collisions at RHIC. As shown in plot (b) of Figure 5, the difference is more pronounced for v_2 of baryons and anti-baryons when the collision energy is less than 20 GeV [78–80]. These differences naturally break the n_q scaling discussed previously, as the number of constituent quarks are same for particle and the corresponding anti-particle. Several models try to explain the data [84–88]: the hydro + transport (UrQMD) calculation can reproduce the proton data, but not the meson data [84]; A analytic hydro model can quantitatively reproduce the π, K and proton data, but the flavor dependence ($\Delta v_2^p > \Delta v_2^\Lambda > \Delta v_2^\Xi > \Delta v_2^\Omega$) is not consistent with data [85]; A Nambu-Jona-Lasino (NJL) model incorporating partonic and hadronic potentials can describe the data qualitatively, but not quantitatively [86,87]. New data from RHIC BES II, especially data of multi-strange hadrons, could offer more constrains on the model calculation.

3. Beam Energy Dependence of the Higher-Order Cumulants of Net-Particle Multiplicity Distributions and Light Nuclei Productions

Fluctuations of conserved quantities, such as net-baryon (B), net-charge (Q) and net-strangeness (S), are sensitive observables to search for the QCD critical point in heavy-ion collisions [89–93]. The higher-order cumulants (C_n, the nth order cumulants), which can be used to quantify the fluctuations and describe the shape of the event-by-event multiplicity distributions, are predicted to be sensitive to the correlation length (ξ) of the system as $C_4 \propto \xi^7$ and $C_3 \propto \xi^{4.5}$ [90,94]. The various order cumulants and cumulant ratios can be expressed in terms of moments as $C_2 = \sigma^2$, $C_3 = S\sigma^3$, $C_4 = \kappa\sigma^4$ and $C_2/C_1 = \sigma^2/M$, $C_3/C_2 = S\sigma$, $C_4/C_2 = \kappa\sigma^2$, where σ^2, S and κ are variance, skewness and kurtosis, respectively [95]. The various order cumulants are extensive quantities and are proportional to the system volume, which is difficult to be measured in heavy-ion collisions. By taking the ratio between various order cumulants, the system volume can be cancelled to the first order and are directly related to the ratios of the thermodynamic susceptibilities (χ) as $C_m/C_n = \chi^{(m)}/\chi^{(n)}$ [89,93,96].

Figure 6 (left) shows the density plot of fourth order cumulant of order parameter as a function of temperature and baryon chemical potential (T and μ_B) by mapping the Ising equation of state onto the QCD equation of state near the critical point [97]. The red and blue regions in the density plot denote the negative and positive contributions to the fourth order cumulant, respectively. Experimentally, by tuning the beam energy, the T and μ_B at chemical freeze-out are varied accordingly. The green dashed line represents the chemical freeze-out points (T, μ_B) passing through the critical region when one varies the beam energies. Figure 6 (right) shows fourth order fluctuation $\kappa\sigma^2$ as a function of baryon chemical potential (μ_B). Due to the negative and positive critical contributions near the critical point, the $\kappa\sigma^2$ will show a non-monotonic energy or μ_B dependence with respect to the non-critical baseline. This is the characteristic experimental signature of the critical point we are looking for in the heavy-ion collision experiment. Theoretically, the properties of QCD phase diagram at finite baryon density and the signatures of conserved charge fluctuations near the QCD critical point have been extensively studied by various model calculations, such as Lattice QCD [10,18–22,98], NJL, PNJL model [99–106], PQM, FRG model [107–109], Dyson-Schwinger Equation (DSE) method [110–113], chiral hydrodynamics [114] and other effective models [94,115–119]. However, one should keep in mind that the above results are under the assumption of thermal equilibrium with infinite and static medium. In the real heavy-ion collisions, there exists the effects of finite size/time [120–122], non-equilibrium [123–127] and thermal blurring effects [128]. Dynamical modeling of heavy-ion collisions by implementing both the critical and those background effects are ongoing [129–131].

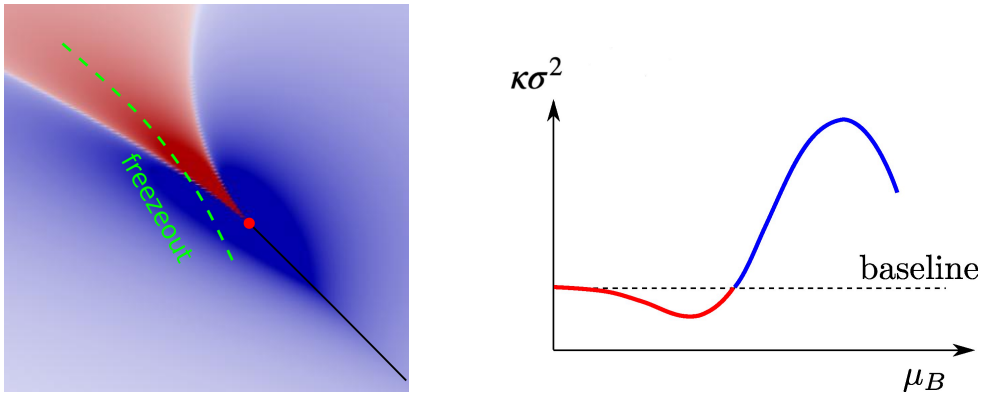

Figure 6. (Color online) (**Left**) Density plot of fourth order cumulant of order parameter as a function of temperature and baryon chemical potential (T and μ_B) by mapping the Ising equation of state onto the QCD equation of state near the critical point [97]. The red and blue regions in the density plot denote the negative and positive contributions to the fourth order cumulant, respectively. The green dashed line is the chemical freeze-out points (T, μ_B) passing through the critical region when we scan the beam energies. (**Right**) Normalized fourth order proton cumulant $\kappa\sigma^2$ as a function of collision energy or μ_B along the chemical freeze-out line.

Before turning to the experimental status, we would like to stress that there is a long history of using the higher-order cumulants to extract the information on that state created in high-energy nuclear collisions. As extensively discussed in Ref. [26], hadron yields or their ratios, which are the first order moment of the multiplicity distributions, have been used for determine the nature of thermalization in such collisions. Once the thermalization is established [132], on the other hand, the higher-orders cumulants of the very same distributions can be used to study the fine structures of the QCD matter. For example, the critical point [94], the nature of the crossover transition [5,107] and the phase boundary [133] at vanishing and large net-baryon region, respectively.

Experimentally, the fluctuation of the net-proton and net-kaon are used as a proxy of net-baryon and net-strangeness fluctuations, respectively. The STAR experiment has measured the higher-order cumulants (C_1–C_4) and second-order off-diagonal cumulants of net-proton [134–139], net-charge [140] and net-kaon [141] multiplicity distributions in Au+Au collisions at $\sqrt{s_{\rm NN}}$= 7.7, 11.5, 14.5, 19.6,

27, 39, 62.4 and 200 GeV, which are collected during the first phase of RHIC beam energy scan program (2010–2014) [142]. To make precise measurements, various corrections and techniques have been applied in the data analysis, those include : (1) Select proper collision centralities to avoid auto-correlations and suppress volume fluctuations [143,144], (2) Detector Efficiency Correction [145–149], (3) Centrality Bin Width Correction (CBWC) [143], (4) Statistical error estimation with Delta theorem and/or Bootstrap [143,150]. Figure 7 shows the measured event-by-event net-charge, net-kaon and net-proton multiplicity distributions of three different centralities in Au+Au collisions at $\sqrt{s_{NN}}$ = 14.5 GeV. Those are raw distributions and not corrected for detector efficiency and acceptance. One should apply the efficiency correction and CBWC to obtain the final efficiency corrected cumulants. In Ref. [150], we have shown that the statistical uncertainties of the cumulants (C_n) strongly depend on the width of the distributions (error $\propto \sigma^n/\sqrt{\mathrm{N}}$). In general, the widths of the distributions in central collisions are wider and with larger mean values than those from peripheral collisions. Further, the widths of the net-charge distributions are much wider than those of net-proton and net-kaon in the same centrality. That's the reason why we observe larger statistical uncertainties in central collisions than those from peripheral. Assuming the measured particles are emitted from many independent sources in the fire ball, the multiplicity distributions in central collisions would be more symmetric and close to Gaussian distribution than the peripheral based on the central limit theorem (CLT). If those sources are identical and uncorrelated, the cumulant ratios are expected to be a constant as a function of collision centralities.

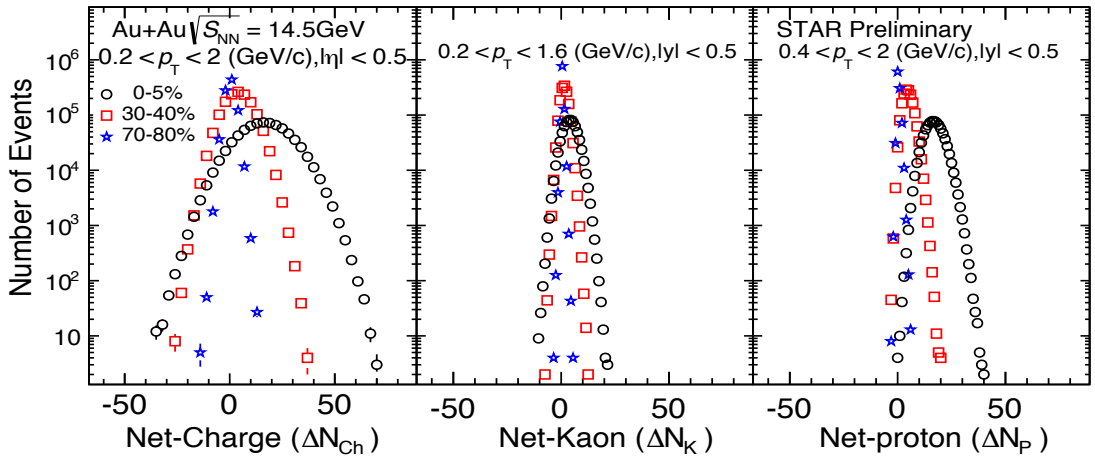

Figure 7. (Color online) The STAR measured raw event-by-event net-charge, net-kaon and net-proton distributions of three centralities (0–5%, 30%–40% and 70%–80%) in Au+Au collisions at $\sqrt{s_{NN}}$ = 14.5 GeV [151].

Figure 8 shows the energy dependence of cumulant ratios (σ^2/M, $S\sigma$/Skellam, $\kappa\sigma^2$) of net-charge, net-kaon and net-proton multiplicity distributions in Au+Au collisions measured by STAR. The blue bands are the results obtained from UrQMD model calculations without including the physics of critical point [92,152,153]. The $S\sigma$ values are normalized by the Skellam expectations, which are constructed with the measured mean values of proton and anti-proton by assuming they are distributed as independent Poisson distributions. The deviation of $S\sigma$/skellam from unity would indicate the deviation of $S\sigma$ from Poisson statistical fluctuations (Poisson baseline). For $S\sigma$/Skellam and $\kappa\sigma^2$, their Poisson baselines are unity, which are plotted as the dashed lines. We found that the σ^2/M of net-charge, net-kaon and net-proton monotonically increase when increasing the collision energy. The $S\sigma$/Skellam and $\kappa\sigma^2$ show weak energy dependence for net-charge and net-kaon measurements. We didn't observe significant deviations of net-charge and net-kaon cumulant ratios $S\sigma$/Skellam and $\kappa\sigma^2$ from the Poisson expectations and UrQMD calculations within uncertainties. However, a clear non-monotonic energy dependence of net-proton $\kappa\sigma^2$ was observed in top 0–5% central Au+Au

collisions. The 0–5% net-proton $\kappa\sigma^2$ values are close to unity for energies above 39 GeV and show large deviations below unity around 19.6 and 27 GeV, and then increasing above unity below 19.6 GeV. The UrQMD calculations of net-proton $\kappa\sigma^2$ displaying a strong suppression below unity at lower energies is due to the effects of baryon number conservation [154–157]. However, this suppression is not observed at low energies in the STAR data. Another transport model (JAM model) study further demonstrates that the resonance weak decay and hadronic re-scattering have very small effects on the proton number fluctuations (C_1–C_4) at low energies [158].

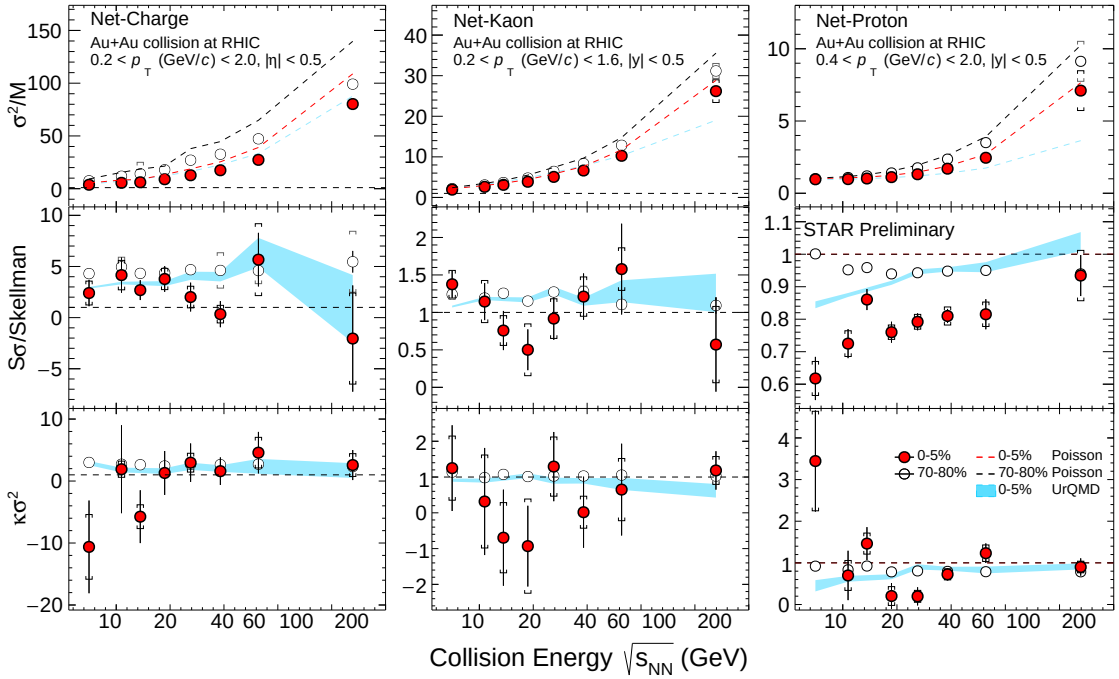

Figure 8. (Color online) Energy dependence of cumulant ratios (σ^2/M, $S\sigma$/Skellam, $\kappa\sigma^2$) of net-charge, net-kaon and net-proton multiplicity distributions for top 0–5% and 70%–80% peripheral collisions. The Poisson expectations are denoted as dotted lines and UrQMD calculations are shown as bands. The statistical and systematical errors are shown in bars and brackets, respectively.

In Figure 9, we summarize the energy dependence of $\kappa\sigma^2$ of net-charge, net-kaon and net-proton multiplicity distributions in Au+Au collisions measured by the STAR experiment. For comparison, the net-charge results in Au+Au collisions at $\sqrt{s_{NN}}$= 7.7, 19.6, 27, 39, 62.4 and 200 GeV measured by the PHENIX experiment [159] are shown in the panel (b). We found that the $\kappa\sigma^2$ of the net-charge and net-kaon multiplicity distributions measured by the STAR experiment show larger statistical uncertainties than those of net-proton $\kappa\sigma^2$. This can be understood as the statistical uncertainties of $\kappa\sigma^2$ depend on the width (σ) of the multiplicity distributions and the particle detecting efficiencies (ϵ) in the detector as $error(C_n/C_2) \propto \sigma^{n-2}/(\sqrt{N}\epsilon^n)$ [146]. The width of the net-charge distributions are larger than those of net-proton and net-kaon. Meanwhile, due to decays, the efficiency of kaon (∼40%) is much lower than proton (∼80%). It is the reason why we observe larger statistical uncertainties for net-kaon fluctuations than net-proton. For the net-charge and net-kaon $\kappa\sigma^2$ from STAR, we observe weak energy dependence within current statistical uncertainties. The PHENIX net-charge $\kappa\sigma^2$ are with much smaller statistical uncertainties than the results from STAR. This is due to smaller acceptance of PHENIX detector than the STAR detector, thus the width of the net-charge multiplicity distributions measured by the PHENIX experiment is much narrower than those measured by STAR. We observe a clear non-monotonic energy dependence for net-proton $\kappa\sigma^2$ in the most central (0–5%) Au+Au collisions with a minimum around 19.6 GeV. This non-monotonic behavior cannot be described by various model calculations without the physics of phase transition and critical point.

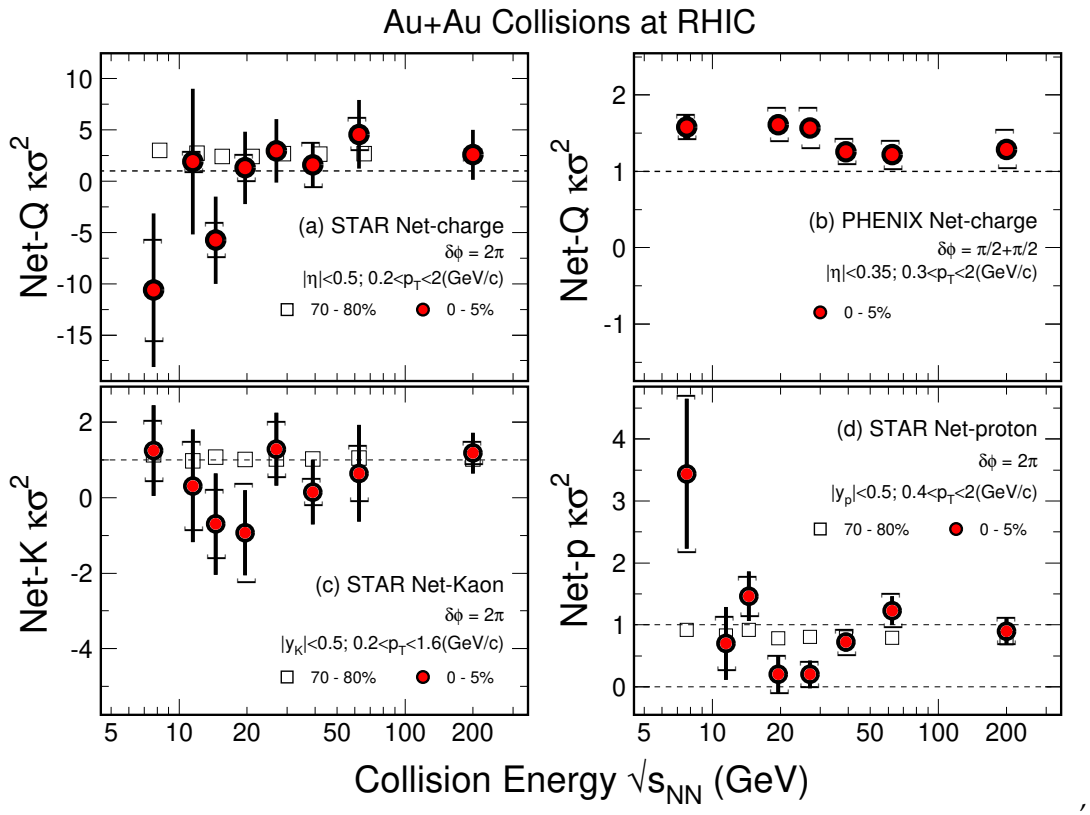

Figure 9. (Color online) The STAR measured energy dependence of $\kappa\sigma^2$ of net-charge (top left), net-kaon and net-proton distributions in Au+Au collisions at $\sqrt{s_{NN}}$ = 7.7, 11.5, 14.5, 19.6, 27, 39, 62.4 and 200 GeV. The net-charge fluctuations measured by the PHENIX experiment in Au+Au collisions at $\sqrt{s_{NN}}$ = 7.7, 19.6, 27, 39, 62.4 and 200 GeV are shown in top right panel.The statistical and systematical errors are shown in bars and brackets, respectively.

Figure 10 shows the energy dependence of the fourth-order fluctuations ($\kappa\sigma^2$) of net-proton from the top 5% central Au+Au collisions measured by STAR experiment [139]. Recent result from the HADES experiment is also shown in the figure. Note that there are differences in the data shown in Figure 10: while STAR data points are from the top 5% central collisions and $|y| < 0.5, 0.4 < p_T < 2.0$ GeV/c, the HADES data is from the top 10% central Au+Au collisions and $|y| < 0.4, 0.4 < p_T < 1.6$ GeV/c. From 200 GeV to 7.7 GeV, non-monotonic energy dependence is clearly shown in the $\kappa\sigma^2$ of net-proton multiplicity distributions and one can observe a strong enhancement at the highest $\mu_B \sim 420$ MeV, corresponding to the Au+Au central collisions at $\sqrt{s_{NN}}$ = 7.7 GeV. This might indicate attractive correlations between nucleons in nature at the large baryon density region. However, interestingly, the strong enhancement in the fourth-order fluctuation seems disappeared as shown by the HADES result at $\sqrt{s_{NN}}$ = 2.4 GeV [160]. Indeed, in the high baryon density region, between $\sqrt{s_{NN}}$ = 2 GeV and 8 GeV, there might be a peak in the fourth order fluctuations as speculated in Ref. [92,97,133]. If the peak structure is confirmed, that would be the experimental indication of the QCD critical point and/or the first order phase transition created in such high-energy nuclear collisions. On the other hand, it is possible that from $\sqrt{s_{NN}}$ = 2 GeV to 8 GeV data points are smoothly connected without any peaks or dips. Results from the future experiments like NICA, CBM, and CEE will certainly provide the answer.

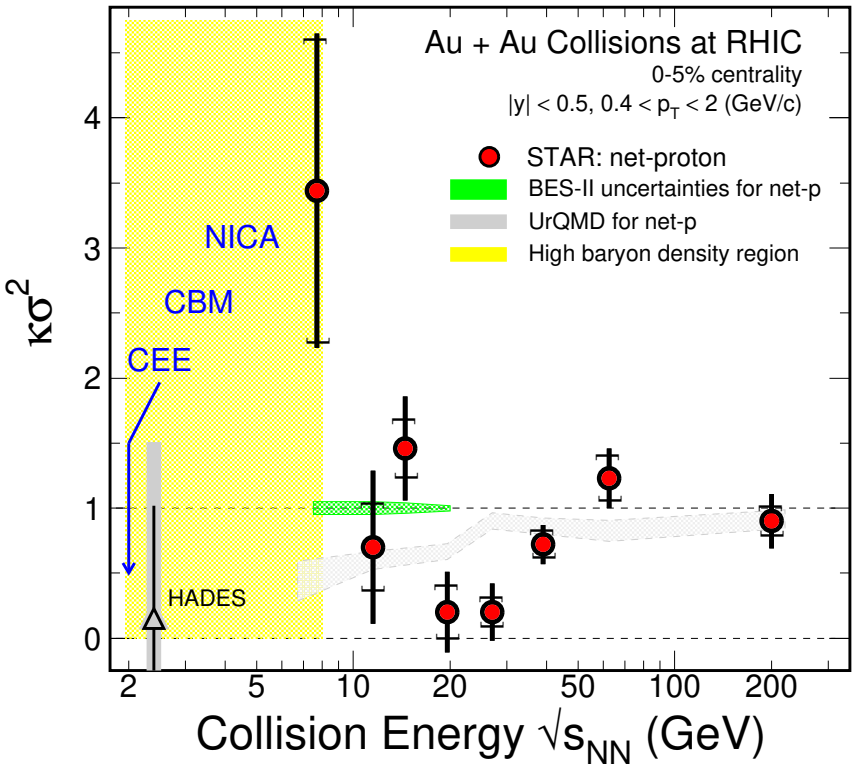

Figure 10. (Color online) Energy dependence of the mid-rapidity net-proton 4th order cumulants ratios from central 0–5% Au+Au collisions, STAR experiment ($|y| < 0.5, 0.4 < p_T < 2.0$ GeV/c: filled-circles) [139] and 0–10% Au+Au collision, HADES experiment ($|y| < 0.4, 0.4 < p_T < 1.6$ GeV/c: open-triangle) [160]. The statistical uncertainties of the second RHIC beam-energy-scan (BES-II) are shown as the green-band while the UrQMD results are shown as gray-band. The energy region covered by the future experiments is shown as yellow.

In Figure 10, the results from the transport model UrQMD (grey band) show a monotonic decrease from low to high baryon density region, which is due to the effect of baryon number conservation in high-energy nuclear collisions. Note that in the Poisson limit, the absence of criticality or other dynamical correlations, the $\kappa\sigma^2$ is expected to be unity. The green band in the figure is the projected statistical error of the fourth-order fluctuations $\kappa\sigma^2$ of net-protons in the second phase of the RHIC Beam Energy Scan (BES-II, 2019–2021) program [161]. The BES-II program, which is scheduled between 2019 and 2021 for the Au+Au collisions at 7.7–19.6 GeV, will take about 10 to 20 times higher statistics (depending on energy) to confirm the non-monotonic behavior observed in the fourth order fluctuations ($\kappa\sigma^2$) of net-proton and proton in Au+Au collisions in the BES-I at RHIC. Assuming the data in the figure is related to the critical region, one must study the net-proton fluctuations at even higher baryon density region, i.e., at lower collision energies. The yellow band shown in the figure represents the high baryon density region ($\sqrt{s_{NN}}$ = 2–8 GeV) covered by future FAIR/CBM fixed target (FXT) experiment ($\sqrt{s_{NN}}$ = 2–5 GeV) [162] and the NICA/MPD collider experiment ($\sqrt{s_{NN}}$ = 4–11 GeV) [163]..

Besides the conserved charge fluctuations, the light nuclei production is predicted to be sensitive to the baryon density fluctuations assuming that the light nuclei is formed from the nucleon coalescence. Model calculations show that the yield ratio between deuteron, triton and proton, $N_t \times N_p / N_d^2$ is related to the neutron density fluctuations, thus can be used to search for the QCD critical point in heavy-ion collisions [164,165]. Experimentally, the STAR experiment has measured the production of deuteron (d) and triton (t) in the Au+Au collisions at $\sqrt{s_{NN}}$ = 7.7, 11.5, 14.5, 19.6, 27, 39, 54.4, 62.4 and 200 GeV. As shown in Figure 11, non-monotonic energy dependence is observed for the yield ratio, $N_t \times N_p / N_d^2$, in 0–10% central Au+Au collisions with a peak around 20–30 GeV [166–168]. The yield

ratios measured by STAR experiment below 20 GeV are consistent with the results calculated from NA49 experiment [164]. Since there is no critical physics implemented in the JAM model, the results of central ($b < 3$ fm) Au+Au collisions from JAM model is also plotted as blue band in Figure 11 for comparison [166]. The model results show a flat energy dependence and cannot describe the non-monotonic trend observed in the STAR data. The current STAR results shown in Figure 11 is for 0–10% centrality, it is also worthwhile to perform centrality dependence study on this yield ratio. On the other hand, more theoretical studies and dynamical modeling of heavy-ion collisions with critical physics are needed to understand whether this non-monotonic behavior is related to the QCD critical fluctuations.

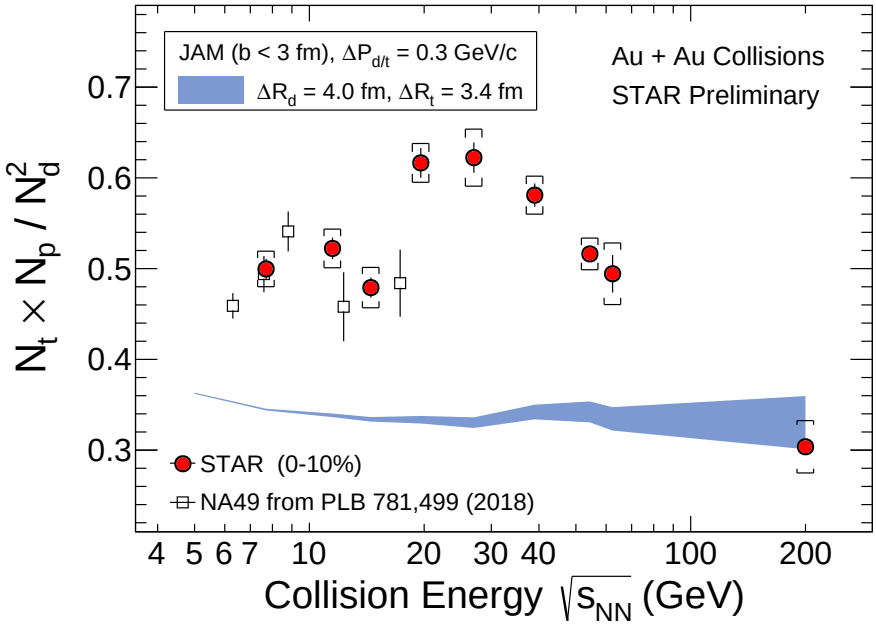

Figure 11. (Color online) Energy dependence of the light nuclei yield ratio $N_t \times N_p / N_d^2$ in central (0–10%) heavy-ion collisions. The red solid circles are the results measured in central (0–10%) Au+Au collisions at BES energies by the STAR experiment and the open squares are the results calculated from the Pb+Pb data of NA49 experiment. The blue band represents the results of central Au+Au collisions ($b < 3$ fm) from the JAM model calculations [166].

4. Beam Energy Dependence of the Heavy-Flavor Production

Since the masses of heavy flavor quarks are much larger than the temperature of the system created in the high-energy nuclear collisions, they can be used as clean probes of the medium properties at early stage of the collisions. As shown in Figure 12, heavy flavor quark masses are all generated in the electro-weak sector while light quarks (u, d, and s) are dominated by the spontaneous breaking of chiral symmetry in QCD. Thus heavy quarks keep massive when participating in strong interactions. Due to their large masses, these heavy flavor quarks are primarily pair-created in initial hard pQCD processes. These facts making heavy quark hadrons are ideal for studying the medium effects including the thermalization of the system. One example has already discussed in previous section, see Figure 3.

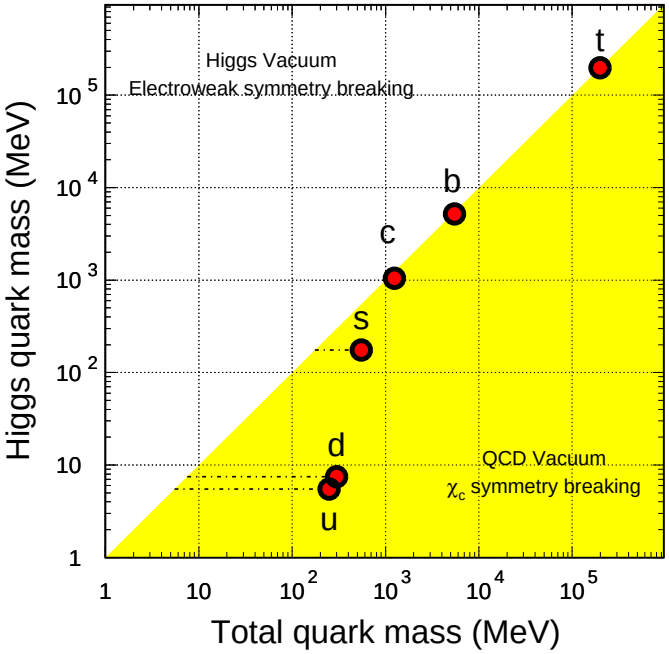

Figure 12. (Color online) Quark masses in the QCD vacuum and the Higgs vacuum. A large fraction of the light quark mass is due the the chiral symmetry breaking in the QCD vacuum. The numerical values were taken from reference [169]. The plot is taken from Ref. [170].

The QCD calculations can evaluate the charm production cross sections at high energies via a perturbation scheme in p+p collisions [171,172]. Figure 13 shows the charm production cross sections at midrapidity as a function of p_{T} in p+p collisions at $\sqrt{s}$ = 7 TeV, 1.96 TeV, 500 GeV and 200 GeV from ALICE [173], CDF [174] and STAR [175,176] experiments, respectively. Within uncertainties the Fixed-Order-Next-to-Leading-Logarithm (FONLL) calculations [172] agree with data. The data points are more on top of the upper limit of the theoretical uncertainties for all of the collision energies.

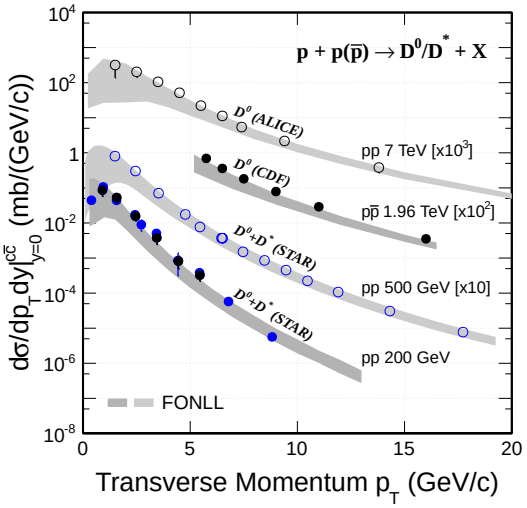

Figure 13. (Color online) Charm production cross sections at midrapidity as a function of p_T. Symbols from top to bottom are experiment results at $\sqrt{s}$ = 7 TeV [173], 1.96 TeV [174], 500 GeV [176] and 200 GeV [175] from ALICE, CDF and STAR experiments, respectively. The gray bands are FONLL calculations with uncertainties.

In heavy-ion collisions, charm quark interacts with the QGP matter when traversing in the medium. The transverse momentum of charm quark is modified by the medium via energy loss or

collective flow. However, the total number of charm quarks may keep conserved since they are produced in initial hard processes before the QGP formation and there is no more charm quark created later via thermal production at RHIC energies. Figure 14 shows the p_T-integrated cross section for D^0 production per nucleon-nucleon collision $d\sigma^{\rm NN}/dy|_{y=0}$ from different centrality bins in $\sqrt{s_{NN}}$ = 200 GeV Au+Au collisions for the full p_T range (a) and for $p_T > 4\,{\rm GeV}/c$ (b), respectively [177]. The result from the p+p measurement at the same collision energy is also shown in both panels [175].

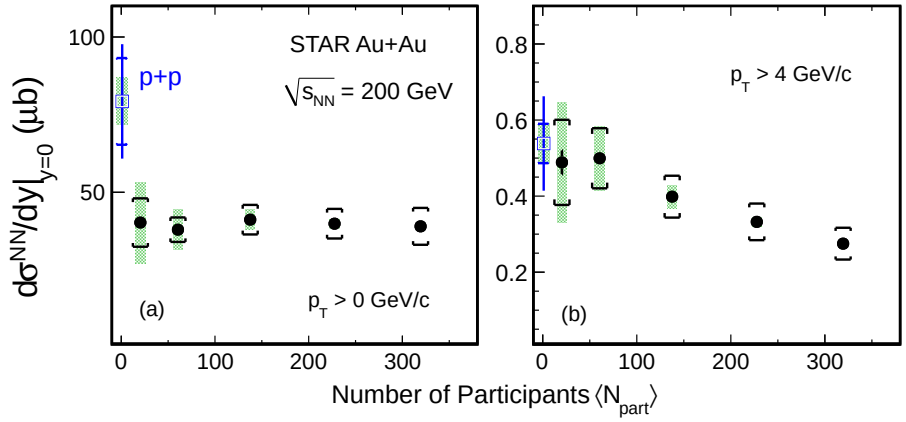

Figure 14. (Color online) Integrated D^0 cross section per nucleon-nucleon collision at mid-rapidity in $\sqrt{s_{NN}}$ = 200 GeV Au+Au collisions for $p_T > 0$ (**a**) and $p_T > 4\,{\rm GeV}/c$ (**b**) as a function of centrality $N_{\rm part}$. The statistical and systematic uncertainties are shown as bars and brackets on the data points. The green boxes on the data points depict the overall normalization uncertainties in p+p and Au+Au data respectively.

The high p_T ($> 4\,{\rm GeV}/c$) $d\sigma^{\rm NN}/dy|_{y=0}$ shows a clear decreasing trend from peripheral to mid-central and central collisions and the result in peripheral collisions is consistent with p+p collisions within uncertainties. This is consistent with charm quarks lose more energy in more central collisions at high p_T. However, for the $d\sigma^{\rm NN}/dy|_{y=0}$ integrated over full p_T range shows approximately a flat distribution as a function of $N_{\rm part}$. The values for the full p_T range in mid-central to central Au+Au collisions are smaller than that in p+p collisions with $\sim$1.5σ effect considering the large uncertainties from the p+p measurements. The total charm quark yield in heavy-ion collisions is expected to follow the number-of-binary-collision scaling since charm quarks are conserved at RHIC energies. However, the cold nuclear matter (CNM) effect including shadowing could also play an important role. In addition, hadronization through coalescence could alter the hadrochemistry distributions of charm quark in various charmed-hadron states which may lead to the reduction in the observed D^0 yields in Au+Au collisions [178]. For instance, hadronization through coalescence can lead to an enhancement of the charmed baryon Λ_c^+ over D^0 yield [179–181], and together with the strangeness enhancement in the hot QCD medium and sequential hadronization, can also lead to an enhancement in the charmed strange meson D_s^+ yield relative to D^0 [180–182].

The STAR Heavy Flavor Tracker (HFT) with a silicon pixel detector achieved $\sim$30 μm spacial resolution of the track impact parameter to the primary vertex allows a topological reconstruction of the decay vertices of open charm hadrons. Figure 15 left panels show the charmed baryon over meson ratio compared with light and strange baryon over meson ratios [183,184] (a) and various models (b). The Λ_c/D^0 ratio is comparable in magnitude to the Λ/K_s^0 and p/π ratios and shows a similar p_T dependence in the measured region. A significant enhancement is seen compared to the calculations from the latest PYTHIA 8.24 release (Monash tune [185]) without (green solid curve) and without (magenta dot-dashed curve) color reconnections (CR) [186]. The implementation with CR is found to enhance the baryon production with respect to mesons. However, both calculations fail to fully describe the data and its p_T dependence. Figure 15b also shows the comparison to various models with coalescence hadronization of charm quarks [179–182]. The comparisons suggest coalescence

hadronization plays an important role in charm-quark hadronization in the presence of QGP. Also, the data can be used to constrain the coalescence model calculations and their model parameters.

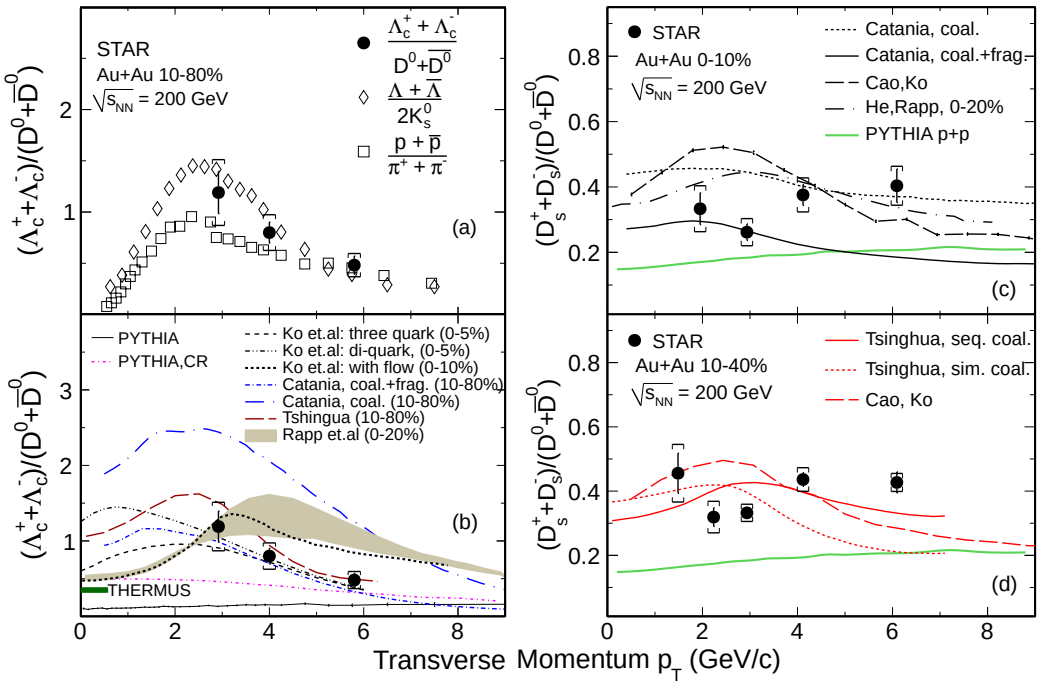

Figure 15. (Color online) Left panels: The measured Λ_c/D^0 ratio at midrapidity ($|y| < 1$) as a function of p_T for Au+Au collisions at $\sqrt{s_{NN}}$ = 200 GeV in 10%–80% centrality, compared to the baryon-to-meson ratios for light and strange hadrons (**a**) and various model calculations (**b**). The p_T-integrated Λ_c/D^0 ratio from the THERMUS [187] model calculation with a freeze-out temperature of $T_{\rm ch} = 160$ MeV is shown as a horizontal bar on the left axis of the plot. Right panels: (**c**) The integrated D_s/D^0 ratio (black solid circles) of $1.5 < p_T < 8$ GeV/c as a function of p_T compared to model calculation (curves) in 0–10%Au+Au collisions at $\sqrt{s_{NN}}$ = 200 GeV. (**d**) Same D_s/D^0 ratio as (c) but with 10–40% centrality. The vertical lines and brackets on the data points indicate statistical and systematic uncertainties respectively.

Figure 15 right panel shows the D_s/D^0 ratio as a function of p_T compared to coalescence model calculations for 0–10% (c) and 10%–40% (d) collision centralities. Several models incorporating coalescence hadronization of charm quarks and strangeness enhancement are used to describe the p_T dependence of D_s/D^0 ratio. Those models assume that $D_s^{\pm}$ mesons are formed by recombination of charm quarks with equilibrated strange quarks in the QGP [179–182]. In particular, the sequential coalescence model together with charm quark conservation [180] considers that more charm quarks are hadronized to $D_s^{\pm}$ mesons than D^0 since the former is created earlier in the QGP, which results in further enhancement of D_s/D^0 ratio in Au+Au collisions relative to $p+p$ collisions.

D meson R_{AA} and v_2 have been observed similar as light flavor hadrons in 200 GeV Au+Au collisions [177], which indicates charm is thermalized in the system with $T \sim$170 MeV. In low energy region, such as the energies in RHIC beam energy scan program, it is of particular interest to measure open charm hadron production in a relative smaller and colder system compared to top energy at 200 GeV. This may provide a chance to tell us in what temperature charm behaves different from light flavors. However, in low energy region, the perturbation algorithm in theoretical calculations of charm production cross section becomes invalid, which may result in large theoretical uncertainties. Meanwhile the charm production cross section drops rapidly when collision energy decreases, it is very challenging to measure open charm production at low energies. The previous measurements at SPS energies are with large uncertainties [188,189]. Since the HFT detector was taken out from STAR for the BES-II runs together with low cross section, it is impossible to reconstruct open charm hadrons

via hadronic decay channels, the electron production from heavy flavor semi-leptonic decays becomes the unique way to measure heavy flavor productions at low energy.

Figure 16 shows the v_2 of electrons from heavy flavor decays as a function of p_T in $\sqrt{s_{\rm NN}} = 54$ and 200 GeV Au+Au collisions [190] as solid circles and open stars, respectively. A semi-empirical exponential function [191] is used to fit all the data points and the ratios of data over the fit function are shown in the bottom panel. The result in 54 GeV agrees with that in 200 GeV within uncertainties, which may suggest charm quarks are still thermalized in 54 GeV Au+Au collisions. On the other hand, it is of interest to repeat the same measurement in lower energies, such as 27 GeV from STAR BESII experiment.

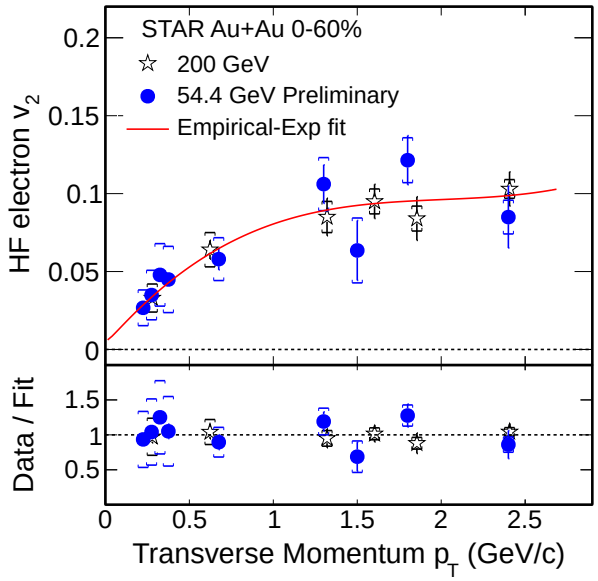

Figure 16. (Color online) Upper panel: v_2 of electrons from heavy flavor decays as a function of p_T in $\sqrt{s_{\rm NN}} = 54$ (blue solid circles) and 200 (open stars) GeV Au+Au collisions [190]. Red curve denotes an empirical reversed exponential fit [191] to all the data points. Bottom panel: The ratios of data over the fit function. Vertical bars and brackets denote statistical and systematic uncertainties, respectively.

STAR experiment extracted the total charm production cross section per binary nucleon collision at midrapidity in $\sqrt{s_{\rm NN}} = 200$ GeV Au+Au collisions by summing all yields of the open charm hadron states and reported as $d\sigma^{\rm NN}/dy|_{y=0}$ = 152 $\pm$ 13 (stat) $\pm$ 29 (sys) μb [192], which is consistent with that in p+p collisions $d\sigma/dy|_{y=0}$ = 130 $\pm$ 30 (stat) $\pm$ 26 (sys) μb [175] within uncertainties. This result is consistent with charm quark conservation in heavy-ion collisions at RHIC top energy.

The total charm production cross section in full rapidity region can be calculated from above charm cross section at midrapidity multiplying an equivalent correction factor (4.7 $\pm$ 0.7) assuming charm quark rapidity distribution from PYTHIA calculations [193]. Figure 17 shows the charm total production cross section over a wide collision energy region from a few ten GeV to TeV. Open symbols are the experimental results taken from Ref. [188,189,194]. STAR p+p [175] and Au+Au [192] results are shown as blue solid square and red star, respectively. As for comparison, the total cross section of charmonium measured from CERN-PS [195], WA39 [196], IHEP [197], E288 [198], E331 [199], E444 [200], E595 [201], E672 [202], E705 [203], E706 [202], E771 [204], E789 [205], NA3 [206], NA38 [207], NA50 [208], NA51 [209], UA6 [210], HERA-B [211], ISR [212], PHENIX [213] experiments (open diamonds) and NRQCD (long-dashed curve) are shown as well over a broad collision energy region [214].

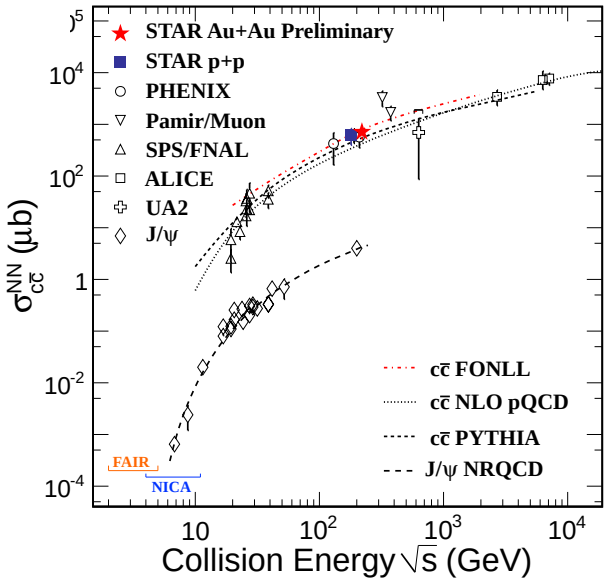

Figure 17. (Color online) Charm and J/ψ total production cross sections per nucleon-nucleon as a function of collision energy. The open diamonds denote the charmonium cross section from worldwide experiments [195–213]. The other open symbols are the experiment results of charm total cross section taken from Ref. [188,189,194]. STAR p+p [175] and Au+Au [192] results are shown as blue solid square and red star, respectively. Model calculations from FONLL [172], NLO pQCD [215], PYTHIA [193] and NRQCD [214] are represented as dot-dashed, dotted, dashed and long-dashed curves, respectively.

5. Future Upgrades and Physics Program at High Baryon Density Region

The RHIC BES program II and future FAIR and NICA experiments will focus on collision energy below 20 GeV offering us a unique opportunity to explore the QCD phase structure at high baryon density region. In Figure 18, interaction rates from both collider experiments and fixed-target experiments are shown. The region for the high baryon density, largely covered by the fixed-target experiments, is highlighted with yellow. In the following, we discuss few key measurements with the future experimental facilities. Again the discussions are arranged around the headlines of Collectivity, Criticality and Heavy Flavor Productions.

Collectivity: The flow results from top energy heavy-ion collisions at RHIC indicate that the partonic collectivity has been built up from light u, d and s quarks to heavy c quark as well. This is one of the most important experimental evidences for the creation of the QGP in high-energy nuclear collisions [1–4]. As a function of the collision energy, both radial and elliptic flow show an increasing trend, say above $\sqrt{s_{NN}} \approx 15$ GeV (Figure 4). Above that energy, the v_1 slope of net-particles for both baryons and mesons, is observed to be almost the same, the v_2 difference between particle and anti-particle also becomes similar (Figure 5). While the dv_1/dy shows large divergence between net-kaon and net-proton (and net-Λ), the particle and anti-particle v_2 difference splits between baryons and mesons dramatically below $\sqrt{s_{NN}} = 15$ GeV, see Figure 5. All of these observations imply that the medium properties created in heavy-ion collisions would be different above/below $\sqrt{s_{NN}} = 15$ GeV.

In collectivity, two noticeable observations are the splitting between baryon's and meson's v_1 and v_2 in the low energy. Mesons such as kaons and $\phi-$mesons are important, especially the $\phi-$meson as it has the similar mass of proton. The precise results of $\phi-$meson's v_1 and v_2 will reveal the origin of collectivity at the high baryon density region. In addition, the ratio of $N(K^-)/N(\phi)$ will shed light on the production mechanism. It could be treated as a micro-laboratory for understanding the quarkonia productions in nucleus-nucleus collisions.

Criticality: One of the main goal of RHIC Beam Energy Scan program is to search for the QCD critical point, which is the end point of the first order phase boundary in the QCD phase diagram. The experimental confirmation of the existence of the CP will be a landmark of exploring

the QCD phase structure. Near the QCD critical point, the density fluctuations and correlation length will diverge. The conserved charge fluctuations and light nuclei productions have been proposed as sensitive observables to search for the signature of QCD phase transition and the QCD critical point. Experimentally, the STAR experiment has measured the higher order cumulants of net-particle distributions and light nuclei productions (deuteron and triton) in Au+Au collisions at $\sqrt{s_{NN}}$ = 7.7 to 200 GeV. In Figures 10 and 11, it has been observed that both fourth order fluctuations of net-proton ($\kappa\sigma^2$) and light nuclei yield ratio $N_t \times N_p / N_d^2$ show non-monotonic energy dependence in central Au+Au collisions, with a minimum and peak around 20 GeV, respectively. Although the two measurements are of different order of fluctuations, the two observations are consistent with the expectation of model calculations with CP physics and might suggest that the created system skims close by the CP receiving the contributions from critical fluctuations. To confirm the above two observed non-monotonic energy dependence trends in BES-I, the second phase of Beam Energy Scan (BES-II) has been planned at RHIC (2019–2021). It will allow us to have 10–20 times more statistics at energies $\sqrt{s_{NN}}$ = 7.7–19.6 GeV. In addition, one observes large changes between 19.6 and 14.5 GeV in the energy dependence of net-proton kurtosis (Figure 10) and light nuclei yield ratio $N_t \times N_p / N_d^2$ (Figure 11) measured in the RHIC BES-I data. This could indicate that the QCD critical point is put by nature between the thermodynamic condition (T, μ_B) of 19.6 and 14.5 GeV. Thus, it is important to conduct a finer beam energy scan between these two energies, i.e., 19.6 GeV (μ_B = 205 MeV) and 14.5 GeV (μ_B = 266 MeV). Therefore, we propose to take the data of a new energy point of Au+Au collisions at $\sqrt{s_{NN}}$ = 16.7 GeV (μ_B = 235 MeV), which is just between 19.6 and 14.5 GeV with equal μ_B gap, on each side. Based on the net-proton fluctuations measured from HADES and STAR experiments, and the model calculations, there might be a peak in the fourth order net-proton fluctuations in Au+Au collisions between $\sqrt{s_{NN}}$ = 2 GeV and 8 GeV. In order to experimentally map out the QCD phase diagram at the higher baryon density region, the future heavy-ion collision experiments like MPD/NICA, CBM/FAIR and CEE/CSR are certainly necessary and important.

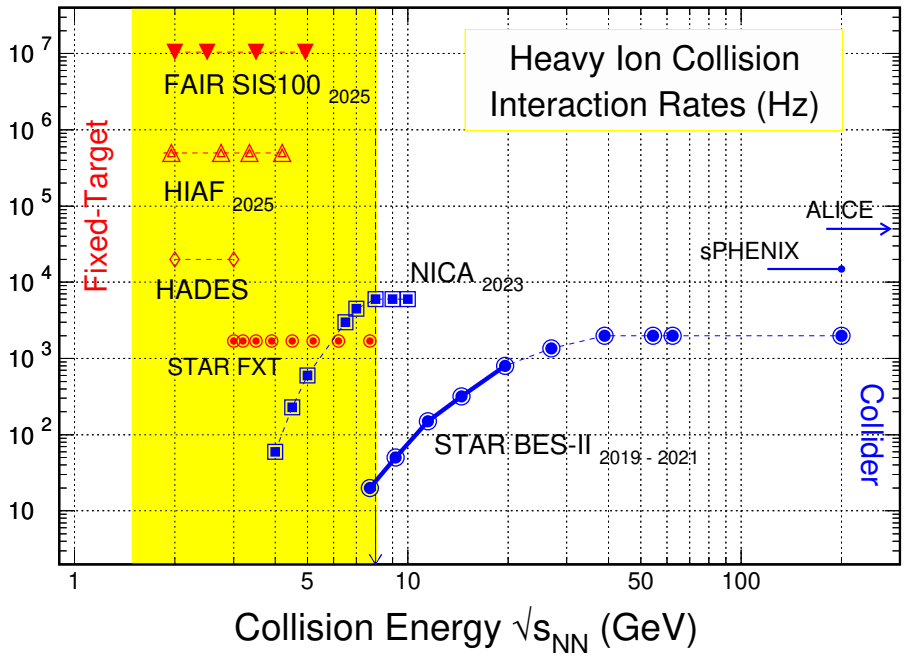

Figure 18. (Color online) Interaction rates for high-energy nuclear collision facilities: the second phase RHIC beam energy scan (filled blue circles: BES-II, 7.7 < $\sqrt{s_{NN}}$ < 19.6 GeV), NICA (squares: 4 < $\sqrt{s_{NN}}$ < 11 GeV) as well as the fixed-target projects including HADES (diamonds), HIAF (triangles) and FAIR (filled triangles). STAR fixed-target range is indicated with filled red circles.

On the other hand, it is predicted that the higher order conserved charge fluctuations, such as sixth order (C_6) or eighth order (C_8) cumulants, should be more sensitive to the phase transition. If the chemical freeze-out temperature in heavy-ion collisions are close enough to the phase boundary, the sixth and eighth order fluctuations could show negative values [98,107]. STAR experiment has measured the centrality dependence of sixth order (C_6/C_2) of net-proton distributions in Au+Au collisions at $\sqrt{s_{NN}}$ = 54.4 and 200 GeV. Negative values are observed for net-proton C_6/C_2 from mid-central to central collisions at 200 GeV, while positive values are observed at 54.4 GeV [216,217]. The negative sign of net-proton C_6/C_2 observed at 200 GeV could be an experimental evidence of smooth crossover at small baryon chemical potential [98,107]. In future fixed target experiments, with much more statistics of low energy data, we can perform precise measurements of those higher order cumulants of conserved charges at the high baryon density region.

Heavy Flavor Production: FAIR-CBM and NICA-MPD experiments with advanced fast detector technology under high luminosity beam condition will provide unique chance to measure open and hidden charm hadrons with large statistics close to the production energy threshold [162,218]. It is expected that this measurements will improve the precision of the total charm cross section at low energies and will provide constraints on pQCD calculations, as well as the unknown interactions between charmed particles and cold hadronic medium. Taking the prediction of the HSD model [219], the yield obtained in one week of running of CBM detectors with 10 MHz event rate would be about 300 J/ψ for central Au+Au collisions at 10A GeV, and about 600 J/ψ for central Ni+Ni collisions at 15A GeV. In the latter case, also open charm production can be studied at a rate of 300 kHz with a silicon vertex detector MVD in operation for charmed hadron decay vertex reconstruction. As a result, the expected yield in central Ni+Ni collisions at 15A GeV will be about 30 D mesons per week. This would be sufficient for cross section measurement and an analysis of charmonium propagation and absorption in dense baryonic matter based on the ratio of hidden to open charm at low energy.

In order to extend the coverage to even larger baryon density region, STAR has developed a fixed-target (FXT) program. As shown in Figure 18, a gold-target (1% interaction length) is placed at the right entrance of TPC. The end cap time-of-flight wall will be constructed at approximately the other side of the TPC entrance. The time-of-flight detectors are on loan from the CBM experiment at FAIR [220,221]. In addition, the inner-TPC upgrade [222] will extend the rapidity coverage, essential for the search for the QCD critical point measurement. STAR will be setup in such a way that data taking from both colliding and FXT modes will take place concurrently. With this configuration, STAR detector system will measure particle productions and correlations in Au+Au collisions from $\sqrt{s_{NN}}$ = 3–19.6 GeV, extending its coverage of baryon chemical potential from about μ_B = 400 MeV to $\mu_B \sim$ 750 MeV. The center of mass energy from the highest energy of the FXT mode is overlay with the lowest colliding mode at $\sqrt{s_{NN}}$ = 7.7 GeV and the lower part of the FXT energies overlap with the future collision energies provided by CBM at FAIR [16]. These allow systematic crosschecks on many of the observables in STAR experiment, for both colliding and FXT modes, and CBM experiment for the FXT mode. The BES program II and future FAIR and NICA experiments will focus on the high baryon density region (<20 GeV), offer us a unique opportunity to explore the QCD phase structure.

In summary, the precise flow measurements of ϕ mesons and multi-strange hadrons with STAR BES-II and future fixed-target experiments will reveal the degree of freedom originates from partonic or hadronic level at the high baryon density region. The confirmation of non-monotonic energy dependence in central Au+Au collisions for net-proton $\kappa\sigma^2$ and/or light nuclei yield ratio $N_t \times N_p / N_d^2$ with STAR BES-II and future fixed-target experiments will provide crucial experimental evidences for establishing the case for the discovery of the QCD critical point. The energy dependence of heavy flavor measurements will provide crucial information on thermalization of the system and provide unique opportunity to study the unknown interactions between heavy quark and the cold nuclear matter. A great deal of new information on the QCD phase diagram will be extracted with current and planned heavy-ion collision programs.

Author Contributions: X.L., S.S., N.X. and Y.Z. contribute equally to this paper. All authors have read and agreed to the published version of the manuscript.

Funding: This work is supported by the National Key Research and Development Program of China (2018YFE0205200), the National Natural Science Foundation of China (No. 11890711, 11890712, 11828501 and 11861131009).

Acknowledgments: We thank Xin Dong, ShinIchi Esumi, Lokesh Kumar, Volker Koch, Bedangadas Mohanty for discussions.

Conflicts of Interest: The authors declare no conflicts of interest.

References

1. Arsene, I.; Bearden, I.; Beavis, D.; Besliu, C.; Budick, B.; Boggild, H.; Chasman, C.; Christensen, C.; Christiansen, P.; Cibor, J.; et al. Quark-gluon plasma and color glass condensate at RHIC? The perspective from the BRAHMS experiment. *Nucl. Phys. A* **2005**, *757*, 1. [CrossRef]
2. Back, B.B.; Baker, M.; Ballintijn, M.; Barton, D.; Becker, B.; Betts, R.; Bickley, A.; Bindel, R.; Budzanowski, A.; Busza, W.; et al. The PHOBOS perspective on discoveries at RHIC. *Nucl. Phys. A* **2005**, *757*, 28. [CrossRef]
3. Adams, J.; Aggarwal, M.; Ahammed, Z.; Amonett, J.; Anderson, B.; Arkhipkin, D.; Averichev, G.; Badyal, S.; Bai, Y.; Balewski, Q.; et al. Experimental and theoretical challenges in the search for the quark–gluon plasma: The STAR Collaboration's critical assessment of the evidence from RHIC collisions. *Nucl. Phys. A* **2005**, *757*, 102. [CrossRef]
4. Adcox, K.; Adler, S.; Afanasiev, S.; Aidala, C.; Ajitanand, N.; Akiba, Y.; Al-Jamel, A.; Alexander, J.; Amirikas, R.; Aoki, K.; et al. Formation of dense partonic matter in relativistic nucleus–nucleus collisions at RHIC: Experimental evaluation by the PHENIX Collaboration. *Nucl. Phys. A* **2005**, *757*, 184. [CrossRef]
5. Aoki, Y.; Endrodi, G.; Fodor, Z.; Katz, S.; Szabo, K. The order of the quantum chromodynamics transition predicted by the standard model of particle physics. *Nature* **2006**, *443*, 675. [CrossRef] [PubMed]
6. Bazavov, A.; Bhattacharya, T.; Cheng, M.; DeTar, C.; Ding, H.; Gottlieb, S.; Gupta, R.; Hegde, P.; Heller, U.; Karsch, F.; et al. The chiral and deconfinement aspects of the QCD transition. *Phys. Rev. D* **2012**, *85*, 054503. [CrossRef]
7. Bazavov, A.; Ding, H.; Hegde, P.; Kaczmarek, O.; Karsch, F.; Karthik, N.; Laermann, E.; Lahiri, A.; Larsen, R.; Li, S.; et al. Chiral crossover in QCD at zero and non-zero chemical potentials. *Phys. Lett. B* **2019**, *795*, 15–21. [CrossRef]
8. Bellwied, R.; Borsanyi, S.; Fodor, Z.; Günther, J.; Katz, S.D.; Ratti, C.; Szabo, K.K. The QCD phase diagram from analytic continuation. *Phys. Lett. B* **2015**, *751*, 559–564. [CrossRef]
9. Borsanyi, S.; Fodor, Z.; Guenther, J.; Kara, R.; Katz, S.; Parotto, P.; Pasztor, A.; Ratti, C.; Szabo, K. The QCD crossover at finite chemical potential from lattice simulations. *arXiv* **2020**, arXiv:2002.02821
10. Bazavov, A.; Ding, H.; Hegde, P.; Kaczmarek, O.; Karsch, F.; Laermann, E.; Mukherjee, S.; Ohno, H.; Petreczky, P.; Rinaldi, E.; et al. Skewness and kurtosis of net baryon-number distributions at small values of the baryon chemical potential. *Phys. Rev. D* **2017**, *96*, 074510. [CrossRef]
11. Bazavov, A.; Ding, H.; Hegde, P.; Kaczmarek, O.; Karsch, F.; Laermann, E.; Maezawa, Y.; Mukherjee, S.; Ohno, H.; Petreczky, P.; et al. QCD equation of state to O(mu(6)(B)) from lattice QCD. *Phys. Rev. D* **2017**, *95*, 054504. [CrossRef]
12. Adamczyk, L.; Adkins, J.; Agakishiev, G.; Aggarwal, M.; Ahammed, Z.; Ajitanand, N.; Alekseev, I.; Anderson, D.; Aoyama, R.; Aparin, A.; et al. Bulk properties of the medium produced in relativistic heavy-ion collisions from the beam energy scan program. *Phys. Rev. C* **2017**, *96*, 044904. [CrossRef]
13. Fukushima, K.; Hatsuda, T. The phase diagram of dense QCD. *Rept. Prog. Phys.* **2011**, *74*, 014001. [CrossRef]
14. Available online: https://drupal.star.bnl.gov/ (accessed on 28 February 2020).
15. Available online: http://nica.jinr.ru/ (accessed on 28 February 2020).
16. Available online: https://fair-center.eu/ (accessed on 28 February 2020).
17. Available online: http://hiaf.impcas.ac.cn/ (accessed on 28 February 2020).
18. Bazavov, A.; Ding, H.; Hegde, P.; Kaczmarek, O.; Karsch, F.; Laermann, E.; Mukherjee, S.; Petreczky, P.; Schmidt, C.; Smith, D.; et al. Freeze-out Conditions in Heavy Ion Collisions from QCD Thermodynamics. *Phys. Rev. Lett.* **2012**, *109*, 192302, doi:10.1103/PhysRevLett.109.192302. [CrossRef] [PubMed]

19. Borsanyi, S.; Fodor, Z.; Katz, S.D.; Krieg, S.; Ratti, C.; Szabo, K.K. Freeze-out parameters from electric charge and baryon number fluctuations: Is there consistency? *Phys. Rev. Lett.* **2014**, *113*, 052301. [CrossRef] [PubMed]
20. Bazavov, A.; Ding, H.; Hegde, P.; Kaczmarek, O.; Karsch, F.; Laermann, E.; Mukherjee, S.; Ohno, H.; Petreczky, P.; Schmidt, C.; et al. Curvature of the freeze-out line in heavy-ion collisions. *Phys. Rev. D* **2016**, *93*, 014512. [CrossRef]
21. Alba, P.; Alberico, W.; Bellwied, R.; Bluhm, M.; Sarti, V.; Nahrgang, M.; Ratti, C. Freeze-out conditions from net-proton and net-charge fluctuations at RHIC. *Phys. Lett. B* **2014**, *738*, 305. [CrossRef]
22. Bluhm, M.; Nahrgang, M. Freeze-out conditions from strangeness observables at RHIC. *Eur. Phys. J. C* **2019**, *79*, 155. [CrossRef]
23. Poberezhnyuk, R.; Vovchenko, V.; Motornenko, A.; Gorenstein, M.I.; Stoecker, H. Chemical freeze-out conditions and fluctuations of conserved charges in heavy-ion collisions within quantum van der Waals model. *Phys. Rev. C* **2019**, *100*, 054904, doi:10.1103/PhysRevC.100.054904. [CrossRef]
24. Alba, P.; Sarti, V.M.; Noronha-Hostler, J.; Parotto, P.; Portillo-Vazquez, I.; Ratti, C.; Stafford, J.M. Influence of hadronic resonances on the chemical freeze-out in heavy-ion collisions. *arXiv* **2020**, arXiv:2002.12395.
25. Acharya, S.; Adamova, D.; Adolfsson, J.; Aggarwal, M.; Aglieri, G.; Agnello, M.; Agrawal, N.; Ahammed, Z.; Ahn, S.; Aiola, S.; et al. Production of 4He and 4$\bar{\text{He}}$ in Pb+Pb collisions at 2.76 TeV at the LHC. *Nucl. Phys. A* **2018**, *971*, 1c. [CrossRef]
26. Andronic, A.; Braun-Munzinger, P.; Redlich, K.; Stachel, J. Decoding the phase structure of QCD via particle production at high energy. *Nature* **2018**, *561*, 321. [CrossRef]
27. Kaczmarek, O.; Karsch, F.; Laermann, E.; Miao, C.; Mukherjee, S.; Petreczky, P.; Schmidt, C.; Soeldner, W.; Unger, W. Phase boundary for the chiral transition in (2+1) -flavor QCD at small values of the chemical potential. *Phys. Rev. D* **2011**, *83*, 014504. [CrossRef]
28. Andronic, A.; Braun-Munzinger, P.; Stachel, J. The horn, the hadron mass spectrum and the QCD phase diagram? The statistical model of hadron production in central nucleus-nucleus collisions. *Nucl. Phys. A* **2010**, *834*, 237c. [CrossRef]
29. Cleymans, J.; Oeschler, H.; Redlich, K.; Wheaton, S.; Comparison of chemical freeze-out criteria in heavy-ion collisions. *Phys. Rev. C* **2006**, *73*, 034905. [CrossRef]
30. Chatterjee, S.; Godbole, R.M.; Gupta, S. Stabilizing hadron resonance gas models. *Phys. Rev. C* **2010**, *81*, 044907. [CrossRef]
31. Adler, C.; Ahammed, Z.; Allgower, C.; Amonett, J.; Anderson, B.; Anderson, M.; Averichev, G.; Balewski, J.; Barannikova, O.; Barnby, L.; et al. Azimuth Anisotropy of K^0_S and $\Lambda + \bar{\Lambda}$ Production at Midrapidity from Au+Au Collisions at $\sqrt{s_{NN}}$ = 130 GeV. *Phys. Rev. Lett.* **2002**, *89*, 132301. [CrossRef]
32. Adams, J.; Aggarwal, M.; Ahammed, Z.; Amonett, J.; Anderson, B.; Arkhipkin, D.; Averichev, G.; Badyal, S.; Bai, Y.; Balewski, Q.; et al. Multistrange Baryon Elliptic Flow in Au + Au Collisions at $\sqrt{s_{NN}}$ = 200 GeV. *Phys. Rev. Lett.* **2005**, *95*, 122301. [CrossRef]
33. Afanasiev, S.; Aidala, C.; Ajitanand, N.; Akiba, Y.; Alexander, J.; Al-Jamel, A.; Aoki, K.; Aphecetche, L.; Armendariz, R.; Aronson, S.; et al. Elliptic Flow for ϕ Mesons and (Anti)deuterons in Au + Au Collisions at $\sqrt{s_{NN}}$ = 200 GeV. *Phys. Rev. Lett.* **2007**, *99*, 052301. [CrossRef]
34. Abelev, B.; Aggarwal, M.; Ahammed, Z.; Anderson, B.; Arkhipkin, D.; Averichev, G.; Bai, Y.; Balewski, J.; Barannikova, O.; Barnby, L.; et al. Partonic Flow and ϕ-Meson Production in Au + Au Collisions at $\sqrt{s_{NN}}$ = 200 GeV. *Phys. Rev. Lett.* **2007**, *99*, 112301. [CrossRef]
35. Abelev, B.; Aggarwal, M.; Ahammed, Z.; Anderson, B.; Arkhipkin, D.; Averichev, G.; Bai, Y.; Balewski, J.; Barannikova, O.; Barnby, L.; et al. Centrality dependence of charged hadron and strange hadron elliptic flow from $\sqrt{s_{NN}}$ = 200 GeV Au + Au collisions. *Phys. Rev. C* **2008**, *77*, 054901. [CrossRef]
36. Abelev, B.; Aggarwal, M.; Ahammed, Z.; Anderson, B.; Arkhipkin, D.; Averichev, G.; Bai, Y.; Balewski, J.; Barannikova, O.; Barnby, L.; et al. Charged and strange hadron elliptic flow in Cu + Cu collisions at $\sqrt{s_{NN}}$ = 62.4 and 200 GeV. *Phys. Rev. C* **2010**, *81*, 044902. [CrossRef]
37. Adamczyk, L.; Adkins, J.; Agakishiev, G.; Aggarwal, M.; Ahammed, Z.; Alekseev, I.; Aparin, A.; Arkhipkin, D.; Aschenauer, E.; Averichev, G.; et al. Centrality and Transverse Momentum Dependence of Elliptic Flow of Multistrange Hadrons and ϕ Meson in Au + Au Collisions at $\sqrt{s_{NN}}$ = 200 GeV. *Phys. Rev. Lett.* **2016**, *116*, 062301. [CrossRef] [PubMed]

38. Adamczyk, L.; Adkins, J.; Agakishiev, G.; Aggarwal, M.; Ahammed, Z.; Ajitanand, N.; Alekseev, I.; Anderson, D.; Aoyama, R.; Aparin, A.; et al. Measurement of D^0 Azimuthal Anisotropy at Midrapidity in Au + Au Collisions at $\sqrt{s_{NN}}$ = 200 GeV. *Phys. Rev. Lett.* **2017**, *118*, 212301. [CrossRef]
39. Schnedermann, E.; Sollfrank, J.; Heinz, U.W. Thermal phenomenology of hadrons from 200A GeV S+S collisions. *Phys. Rev. C* **1993**, *48*, 2462. [CrossRef]
40. Akiba, Y.; Ahle, L.; Akiba, Y.; Ashktorab, K.; Baker, M.; Beavis, D.; Britt, H.; Chang, J.; Chasman, C.; Chen, Z.; et al. Particle production in Au + Au collisions from BNL E866. *Nucl. Phys. A* **1996**, *610*, 139c. [CrossRef]
41. Ahle, L.; Akiba, Y.; Ashktorab, K.; Baker, M.; Beavis, D.; Britt, H.; Chang, J.; Chasman, C.; Chen, Z.; Chi, C.; et al. Particle production at high baryon density in central Au+Au reactions at 11.6A GeV/c. *Phys. Rev. C* **1998**, *57*, R466. [CrossRef]
42. Ahle, L.; Akiba, Y.; Ashktorab, K.; Baker, M.; Beavis, D.; Britt, H.; Chang, J.; Chasman, C.; Chen, Z.; Chi, C.; et al. Proton and deuteron production in Au+Au reactions at 11.6A GeV/c. *Phys. Rev. C* **1999**, *60*, 064901. [CrossRef]
43. Ahle, L.; Akiba, Y.; Ashktorab, K.; Baker, M.; Beavis, D.; Beery, P.; Britt, H.; Budick, B.; Chang, J.; Chasman, C.; et al. Centrality dependence of kaon yields in Si+A and Au+Au collisions at relativistic energies. *Phys. Rev. C* **1999**, *60*, 044904. [CrossRef]
44. Ahle, L.; Akiba, Y.; Ashktorab, K.; Baker, M.; Beavis, D.; Budick, B.; Chang, J.; Chasman, C.; Chen, Z.; Chu, Y.; et al. Excitation function of K^+ and π^+ production in Au+Au reactions at 2-10 AGeV. *Phys. Lett. B* **2000**, *476*, 1. [CrossRef]
45. Ahle, L.; Akiba, Y.; Ashktorab, K.; Baker, M.; Beavis, D.; Budick, B.; Chang, J.; Chasman, C.; Chen, Z.; Chu, Y.; et al. An excitation function of K^- and K^+ production in Au+Au reactions at the AGS. *Phys. Lett. B* **2000**, *490*, 53. [CrossRef]
46. Barrette, J.; Bellwied, R.; Bennett, S.; Bersch, R.; Braun-Munzinger, P.; Chang, W.; Cleland, W.; Clemen, M.; Cole, J.; Cormier, T.; et al. Proton and pion production in Au+Au collisions at 10.8A GeV/c. *Phys. Rev. C* **2000**, *62*, 024901. [CrossRef]
47. Klay, J.; Ajitanand, N.; Alexander, J.; Anderson, M.; Best, D.; Brady, F.; Case, T.; Caskey, W.; Cebra, D.; Chance, J.; et al. Longitudinal Flow of Protons from (2-8)A GeV Collisions. *Phys. Rev. Lett.* **2002**, *88*, 102301. [CrossRef] [PubMed]
48. Afanasiev, S.; Anticic, T.; Barna, D.; Bartke, J.; Barton, R.; Behler, M.; Betev, L.; Bialkowska, H.; Billmeier, A.; Blume, C.; et al. Energy dependence of pion and kaon production in central Pb+Pb collisions. *Phys. Rev. C* **2002**, *66*, 054902. [CrossRef]
49. Anticic, T.; Baatar, B.; Barna, D.; Bartke, J.; Behler, M.; Betev, L.; Bialkowska, H.; Billimeier, A.; Blume, C.; Boimska, B.; et al. Energy and centrality dependence of deuteron and proton production in Pb+Pb collisions at relativistic energies. *Phys. Rev. C* **2004**, *69*, 024902. [CrossRef]
50. Alt, C.; Anticic, T.; Baatar, B.; Barna, D.; Bartke, J.; Betev, L.; Bialkowska, H.; Blume, C.; Boimska, B.; Botje, M.; et al. Energy and centrality dependence of p and $\bar{p}$ production and the $\bar{\Lambda}/\bar{p}$ ratio in Pb+Pb collisions between 20A GeV and 158A GeV. *Phys. Rev. C* **2006**, *73*, 044910. [CrossRef]
51. Alt, C.; Anticic, T.; Baatar, B.; Barna, D.; Bartke, J.; Betev, L.; Bialkowska, H.; Blume, C.; Boimska, B.; Botje, M.; et al. Pion and kaon production in central Pb+Pb collisions at 20A and 30A GeV: Evidence for the onset of deconfinement. *Phys. Rev. C* **2008**, *77*, 024903. [CrossRef]
52. Abelev, B.; Aggarwal, M.; Ahammed, Z.; Anderson, B.; Arkhipkin, D.; Averichev, G.; Bai, Y.; Balewski, J.; Barannikova, O.; Barnby, L.; et al. Systematic measurements of identified particle spectra in pp, d+Au, and Au+Au collisions at the STAR detector. *Phys. Rev. C* **2009**, *79*, 034909. [CrossRef]
53. Adam, J.; Adamczyk, L.; Adams, J.; Adkins, J.; Agakishiev, G.; Aggarwal, M.; Ahammed, Z.; Alekseev, I.; Anderson, D.; et al. Bulk Properties of the System Formed in Au+Au Collisions at $\sqrt{s_{NN}}$ = 14.5 GeV at STAR. *arXiv* **2019**, arXiv:1908.03585v1.
54. Abelev, B.; Adam, J.; Adamova, D.; Adare, A.; Aggarwal, M.; Aglieri, G.; Agnello, M.; Agocs, A.; Agostinelli, A.; Ahammed, Z.; et al. Centrality dependence of π, K and p production in Pb-Pb collisions at $\sqrt{s_{NN}}$ = 2.76 TeV. *Phys. Rev. C* **2013**, *88*, 044910. [CrossRef]
55. Pinkenburg, C.; Ajitanand, N.; Alexander, J.; Anderson, M.; Best, D.; Brady, F.; Case, T.; Caskey, W.; Cebra, D.; Chance, J.; et al. Elliptic Flow: Transition from Out-of-Plane to In-Plane Emission in Au+Au Collisions. *Phys. Rev. Lett.* **1999**, *83*, 1295. [CrossRef]

56. Alt, C.; Anticic, T.; Baatar, B.; Barna, D.; Bartke, J.; Behler, M.; Betev, L.; Bialkowska, H.; Billimeier, A.; Blume, C.; et al. Directed and elliptic flow of charged pions and protons in Pb+Pb collisions at 40A and 158A GeV. *Phys. Rev. C* **2003**, *68*, 034903. [CrossRef]
57. Andronic, A.; Barret, V.; Basrak, Z.; Bastid, N.; Benabderrahmane, L.; Berek, G.; Caplar, R.; Cordier, P.; Crochet, P.; Dupieux, P.; et al. Excitation function of elliptic flow in Au + Au collisions and the nuclear matter equation of state. *Phys. Lett. B* **2005**, *612*, 173. [CrossRef]
58. Braun-Munzinger, P.; Stachel, J. Dynamics of ultra-relativistic nuclear collisions with heavy beams: An experimental overview. *Nucl. Phys. A* **1998**, *638*, 3c. [CrossRef]
59. Appelshauser, H. New results from CERES. *Nucl. Phys. A* **2002**, *698*, 253c. [CrossRef]
60. Aamodt, K.; Abelev, B.; Abrahantes, A.; Adamova, D.; Adare, A.; Aggarwal, M.; Aglieri, G.; Agocs, A.; Aguilar, S.; Ahammed, Z.; et al. Elliptic Flow of Charged Particles in Pb+Pb Collisions at $\sqrt{s_{NN}}$ = 2.76 TeV. *Phys. Rev. Lett.* **2010**, *105*, 252302. [CrossRef]
61. Voloshin, S.A.; Poskanzer, A.M.; Snellings, R. Collective phenomena in non-central nuclear collisions. In *Relativistic Heavy Ion Physics*; Springer: Berlin/Heidelberg, Germany, 2010; pp. 293–333.
62. Adams, J.; Aggarwal, M.; Ahammed, Z.; Amonett, J.; Anderson, B.; Arkhipkin, D.; Averichev, G.; Badyal, S.; Bai, Y.; Balewski, Q.; et al. Azimuthal anisotropy in Au+Au collisions at $\sqrt{s_{NN}}$ = 200 GeV. *Phys. Rev. C* **2005**, *72*, 014904. [CrossRef]
63. Adler, C.; Ahammed, Z.; Allgower, C.; Amonett, J.; Anderson, B.; Anderson, M.; Averichev, G.; Balewski, J.; Barannikova, O.; Barnby, L.; et al. Elliptic flow from two- and four-particle correlations in Au+Au collisions at $\sqrt{s_{NN}}$ = 130 GeV. *Phys. Rev. C* **2002**, *66*, 034904. [CrossRef]
64. Adare, A.; Afanasiev, S.; Aidala, C.; Ajitanand, N.; Akiba, Y.; Al-Bataineh, H.; Alexander, J.; Al-Jamel, A.; Aoki, K.; Aphecetche, L.; et al. Scaling Properties of Azimuthal Anisotropy in Au+Au and Cu+Cu Collisions at $\sqrt{s_{NN}}$ = 200 GeV. *Phys. Rev. Lett.* **2007**, *98*, 162301. [CrossRef]
65. Alver, B.; Back, B.; Baker, M.; Ballintijn, M.; Barton, D.; Betts, R.; Bickley, A.; Bindel, R.; Busza, W.; Carroll, A.; et al. System Size, Energy, Pseudorapidity, and Centrality Dependence of Elliptic Flow. *Phys. Rev. Lett.* **2007**, *98*, 242302. [CrossRef]
66. Adamczyk, L.; Agakishiev, G.; Aggarwal, M.; Ahammed, Z.; Alakhverdyants, A.; Alekseev, I.; Alford, J.; Anderson, B.; Anson, C.; Arkhipkin, D.; et al. Inclusive charged hadron elliptic flow in Au+Au collisions at $\sqrt{s_{NN}}$ = 7.7–39 GeV. *Phys. Rev. C* **2012**, *86*, 054908. [CrossRef]
67. Shi, S. Event anisotropy v_2 in Au+Au collisions at $\sqrt{s_{NN}}$ = 7.7–62.4 GeV with STAR. *Nucl. Phys. A* **2013**, *904-905*, 895c. [CrossRef]
68. Kolb, P.F.; Sollfrank, J.; Heinz, U. Anisotropic transverse flow and the quark-hadron phase transition. *Phys. Rev. C* **2000**, *62*, 054909. [CrossRef]
69. Sorge, H. Highly Sensitive Centrality Dependence of Elliptic Flow: A Novel Signature of the Phase Transition in QCD. *Phys. Rev. Lett.* **1999**, *82*, 2048. [CrossRef]
70. Heinz, U.W. *Relativistic Heavy Ion Physics*; Stock, R., Ed.; Landolt- Bornstein Data Collection Series; Springer: New York, NY, USA, 2010; Volume I/23.
71. Bass, S.; Belkacem, M.; Bleicher, M.; Brandstetter, M.; Bravina, L.; Ernst, C.; Gerland, L.; Hofmann, M.; Hofmann, S.; Konopka, J.; et al. Microscopic models for ultrarelativistic heavy ion collisions. *Prog. Part. Nucl. Phys.* **1998**, *41*, 255. [CrossRef]
72. Bleicher, M.; Zabrodin, E.; Spieles, C.; Bass, S.; Ernst, C.; Soff, S.; Bravina, L.; Belkacem, M.; Weber, H.; Stocker, H.; et al. Relativistic Hadron-Hadron Collisions in the Ultra-Relativistic Quantum Molecular Dynamics Model (UrQMD). *J. Phys. G* **1999**, *25*, 1859. [CrossRef]
73. Rischke, D.; Maruhn, J.; Stocker, H.; Greiner, W. The phase transition to the quark-gluon plasma and its effect on hydrodynamic flow. *Heavy Ion Phys.* **1996**, *1*, 309.
74. Stocker, H. Collective flow signals the quark gluon plasma. *Nucl. Phys. A* **2005**, *750*, 121. [CrossRef]
75. Adamczyk, L.; Adkins, J.; Agakishiev, G.; Aggarwal, M.; Ahammed, Z.; Alekseev, I.; Alford, J.; Anson, C.; Aparin, A.; Arkhipkin, D.; et al. Beam-Energy Dependence of the Directed Flow of Protons, Antiprotons, and Pions in Au+Au Collisions. *Phys. Rev. Lett.* **2014**, *112*, 162301. [CrossRef]
76. Adamczyk, L.; Adam, J.; Adamczyk, L.; Adams, J.; Adkins, J.; Agakishiev, G.; Aggarwal, M.; Ahammed, Z.; Ajitanand, N.; Alekseev, I.; et al. Beam-Energy Dependence of Directed Flow of Λ, $\bar{\Lambda}$, $K^{\pm}$, K^0_s, and ϕ in Au+Au Collisions. *Phys. Rev. Lett.* **2018**, *120*, 062301. [CrossRef]

77. Nayak, K.; Shi, S.; Xu, N.; Lin, Z.-W. Energy dependence study of directed flow in Au+Au collisions using an improved coalescence in a multiphase transport model. *Phys. Rev. C* **2019**, *100*, 054903. [CrossRef]
78. Adamczyk, L.; Adkins, J.; Agakishiev, G.; Aggarwal, M.; Ahammed, Z.; Alekseev, I.; Alford, J.; Anson, C.; Aparin, A.; Arkhipkin, D.; et al. Observation of an Energy-Dependent Difference in Elliptic Flow between Particles and Antiparticles in Relativistic Heavy Ion Collisions. *Phys. Rev. Lett.* **2013**, *110*, 142301. [CrossRef] [PubMed]
79. Adamczyk, L.; Adkins, J.; Agakishiev, G.; Aggarwal, M.; Ahammed, Z.; Alekseev, I.; Alford, J.; Anson, C.; Aparin, A.; Arkhipkin, D.; et al. Elliptic flow of identified hadrons in Au + Au collisions at $\sqrt{s_{NN}}$ = 7.7–62.4 GeV. *Phys. Rev. C* **2013**, *88*, 014902. [CrossRef]
80. Adamczyk, L.; Adkins, J.; Agakishiev, G.; Aggarwal, M.; Ahammed, Z.; Alekseev, I.; Aparin, A.; Arkhipkin, D.; Aschenauer, E.; Averichev, G.; et al. Centrality dependence of identified particle elliptic flow in relativistic heavy-ion collisions at $\sqrt{s_{NN}}$ = 7.7–62.4 GeV. *Phys. Rev. C* **2016**, *93*, 014907. [CrossRef]
81. Shor, A. ϕ-Meson production as a probe of the quark-gluon plasma. *Phys. Rev. Lett.* **1985**, *54*, 1122. [CrossRef]
82. van Hecke, H.; Sorge, H.; Xu, N. Evidence of early mul- tistrange hadron freeze-out in high energy nuclear collisions. *Phys. Rev. Lett.* **1998**, *81*, 5764. [CrossRef]
83. Shi, S. An Experimental Review on Elliptic Flow of Strange and Multistrange Hadrons in Relativistic Heavy Ion Collisions. *Adv. High Energy Phys.* **2016**, *2016*, 1987432. [CrossRef]
84. Steinheimer, J.; Koch, V.; Bleicher, M. Hydrodynamics at large baryon densities: Understanding proton versus anti-proton v_2 and other puzzles. *Phys. Rev. C* **2012**, *86*, 044903. [CrossRef]
85. Hatta, Y.; Monnai, A.; Xiao, B.-W. Flow harmonics v_n at finite density. *Phys. Rev. D* **2015**, *92*, 114010. [CrossRef]
86. Xu, J.; Song, T.; Ko, C.; Li, F. Elliptic flow splitting as a probe of the QCD phase structure at finite baryon chemical potential. *Phys. Rev. Lett.* **2014**, *112*, 012301. [CrossRef]
87. Liu, H.; Wang, F.; Sun, K.; Xu, J.; Ko, C. Isospin splitting of pion elliptic flow in relativistic heavy-ion collisions. *Phys. Lett. B* **2019**, *798*, 135002. [CrossRef]
88. Biao, T.; Shi, S.; Liu, F. Elliptic flow of transported and produced protons in Au+Au collisions with the UrQMD model. *Chin. Rhys. C* **2019**, *43*, 054106.
89. Ejiri, S.; Karsch, F.; Redlich, K. Hadronic fluctuations at the QCD phase transition. *Phys. Lett. B* **2006**, *633*, 275–283. [CrossRef]
90. Stephanov, M.A. Non-Gaussian fluctuations near the QCD critical point. *Phys. Rev. Lett.* **2009**, *102*, 032301. [CrossRef]
91. Asakawa, M.; Ejiri, S.; Kitazawa, M. Third moments of conserved charges as probes of QCD phase structure. *Phys. Rev. Lett.* **2009**, *103*, 262301. [CrossRef]
92. Luo, X.; Xu, N. Search for the QCD Critical Point with Fluctuations of Conserved Quantities in Relativistic Heavy-Ion Collisions at RHIC : An Overview. *Nucl. Sci. Tech.* **2017**, *28*, 112. [CrossRef]
93. Gupta, S.; Luo, X.; Mohanty, B.; Ritter, H.G.; Xu, N. Scale for the Phase Diagram of Quantum Chromodynamics. *Science* **2011**, *332*, 1525, doi:10.1126/science.1204621. [CrossRef]
94. Stephanov, M.A. On the sign of kurtosis near the QCD critical point. *Phys. Rev. Lett.* **2011**, *107*, 052301. [CrossRef]
95. Kitazawa, M.; Luo, X. Properties and uses of factorial cumulants in relativistic heavy-ion collisions. *Phys. Rev. C* **2017**, *96*, 024910. [CrossRef]
96. Ding, H.T.; Karsch, F.; Mukherjee, S. Thermodynamics of strong-interaction matter from Lattice QCD. *Int. J. Mod. Phys. E* **2015**, *24*, 1530007. [CrossRef]
97. A Bzdak; Esumi, S.; Koch, V.; Liao, J.; Stephanov, M.; Xu, N. Mapping the Phases of Quantum Chromodynamics with Beam Energy Scan. *arXiv* **2019**, arXiv:1906.00936.
98. Bazavov, A.; Bollweg, D.; Ding, H.; Enns, P.; Goswami, J.; Hegde, P.; Kaczmarek, O.; Karsch, F.; Larsen, R.; Mukherjee, S.; et al. Skewness, kurtosis and the 5th and 6th order cumulants of net baryon-number distributions from lattice QCD confront high-statistics STAR data. *arXiv* **2020**, arXiv:2001.08530.
99. Fu, W.J.; Liu, Y.X.; Wu, Y.L. Fluctuations and Correlations of Conserved Charges in QCD at Finite Temperature with Effective Models. *Phys. Rev. D* **2010**, *81*, 014028. [CrossRef]
100. Fu, W.J.; Wu, Y.L. Fluctuations and Correlations of Conserved Charges near the QCD Critical Point. *Phys. Rev. D* **2010**, *82*, 074013. [CrossRef]

101. Lu, Y.; Du, Y.; Cui, Z.F.; Zong, H.S. Critical behaviors near the (tri-)critical end point of QCD within the NJL model. *Eur. Phys. J. C* **2015**, *75*, 495. [CrossRef]
102. Chen, J.W.; Deng, J.; Kohyama, H.; Labun, L. Robust characteristics of nongaussian fluctuations from the NJL model. *Phys. Rev. D* **2016**, *93*, 034037. [CrossRef]
103. Fan, W.; Luo, X.; Zong, H.S. Mapping the QCD phase diagram with susceptibilities of conserved charges within Nambu–Jona-Lasinio model. *Int. J. Mod. Phys. A* **2017**, *32*, 1750061. [CrossRef]
104. Fan, W.; Luo, X.; Zong, H. Probing the QCD phase structure with higher order baryon number susceptibilities within the NJL model. *Chin. Phys. C* **2019**, *43*, 033103. [CrossRef]
105. Li, Z.; Xu, K.; Wang, X.; Huang, M. The kurtosis of net baryon number fluctuations from a realistic Polyakov–Nambu–Jona-Lasinio model along the experimental freeze-out line. *Eur. Phys. J. C* **2019**, *79*, 245. [CrossRef]
106. Yang, L.K.; Luo, X.; Zong, H.S. QCD phase diagram in chiral imbalance with self-consistent mean field approximation. *Phys. Rev. D* **2019**, *100*, 094012. [CrossRef]
107. Friman, B.; Karsch, F.; Redlich, K.; Skokov, V. Fluctuations as probe of the QCD phase transition and freeze-out in heavy-ion collisions at LHC and RHIC. *Eur. Phys. J. C* **2011**, *71*, 1694 [CrossRef]
108. Fu, W.J.; Pawlowski, J.M.; Rennecke, F.; Schaefer, B.J. Baryon number fluctuations at finite temperature and density. *Phys. Rev. D* **2016**, *94*, 116020. [CrossRef]
109. Fu, W.J.; Pawlowski, J.M.; Rennecke, F. The QCD phase structure at finite temperature and density. *arXiv* **2019**, arXiv:1909.02991.
110. Fischer, C.S.; Luecker, J. Propagators and phase structure of Nf=2 and Nf=2+1 QCD. *Phys. Lett. B* **2013**, *718*, 1036. [CrossRef]
111. Shi, C.; Wang, Y.L.; Jiang, Y.; Cui, Z.F.; Zong, H.S. Locate QCD Critical End Point in a Continuum Model Study. *JHEP* **2014**, *1407*, 14. [CrossRef]
112. Gao, F.; Liu, Y.X. QCD phase transitions via a refined truncation of Dyson-Schwinger equations. *Phys. Rev. D* **2016**, *94*, 076009. [CrossRef]
113. Fischer, C.S. QCD at finite temperature and chemical potential from Dyson–Schwinger equations. *Prog. Part. Nucl. Phys.* **2019**, *105*, 1. [CrossRef]
114. Herold, C.; Nahrgang, M.; Yan, Y.; Kobdaj, C. Dynamical net-proton fluctuations near a QCD critical point. *Phys. Rev. C* **2016**, *93*, 021902. [CrossRef]
115. Chen, J.W.; Deng, J.; Labun, L. Baryon susceptibilities, non-Gaussian moments, and the QCD critical point. *Phys. Rev. D* **2015**, *92*, 054019. [CrossRef]
116. Vovchenko, V.; Anchishkin, D.V.; Gorenstein, M.I.; Poberezhnyuk, R.V. Scaled variance, skewness, and kurtosis near the critical point of nuclear matter. *Phys. Rev. C* **2015**, *92*, 054901. [CrossRef]
117. Jiang, L.; Li, P.; Song, H. Correlated fluctuations near the QCD critical point. *Phys. Rev. C* **2016**, *94*, 024918. [CrossRef]
118. Mukherjee, A.; Steinheimer, J.; Schramm, S. Higher-order baryon number susceptibilities: Interplay between the chiral and the nuclear liquid-gas transitions. *Phys. Rev. C* **2017**, *96*, 025205 [CrossRef]
119. Zhang, H.; Hou, D.; Kojo, T.; Qin, B. Functional renormalization group study of the quark-meson model with ω meson. *Phys. Rev. D* **2017**, *96*, 114029. [CrossRef]
120. Palhares, L.F.; Fraga, E.S.; Kodama, T. Finite-size effects and signatures of the QCD critical endpoint. *J. Phys. G* **2010**, *37*, 094031. [CrossRef]
121. Fraga, E.S.; Palhares, L.F.; Sorensen, P. Finite-size scaling as a tool in the search for the QCD critical point in heavy ion data. *Phys. Rev. C* **2011**, *84*, 011903. [CrossRef]
122. Pan, Z.; Cui, Z.F.; Chang, C.H.; Zong, H.S. Finite-volume effects on phase transition in the Polyakov-loop extended Nambu–Jona-Lasinio model with a chiral chemical potential. *Int. J. Mod. Phys. A* **2017**, *32*, 1750067. [CrossRef]
123. Mukherjee, S.; Venugopalan, R.; Yin, Y. Universal off-equilibrium scaling of critical cumulants in the QCD phase diagram. *Phys. Rev. Lett.* **2016**, *117*, 222301. [CrossRef]
124. Bluhm, M.; Nahrgang, M.; Kalweit, A.; Arslandok, M.; Braun-Munzinger, P.; Floerchinger, S.; Fraga, E.; Gazdzicki, M.; Hartnack, C.; Herold, C.; et al. Dynamics of critical fluctuations: Theory – phenomenology – heavy-ion collisions. *arXiv* **2020**, arXiv:2001.08831.
125. Wu, S.; Wu, Z.; Song, H. Universal scaling of the σ field and net-protons from Langevin dynamics of model A. *Phys. Rev. C* **2019**, *99*, 064902. [CrossRef]

126. Nahrgang, M.; Bluhm, M.; Schaefer, T.; Bass, S. Diffusive dynamics of critical fluctuations near the QCD critical point. *Phys. Rev. D* **2019**, *99*, 116015. [CrossRef]
127. Asakawa, M.; Kitazawa, M.; Müller, B. Note on Search for Critical Point in QCD with Relativistic Heavy Ion Collisions. *arXiv* **2019**, arXiv:1912.05840.
128. Ohnishi, Y.; Kitazawa, M.; Asakawa, M. Thermal blurring of event-by-event fluctuations generated by rapidity conversion. *Phys. Rev. C* **2016**, *94*, 044905. [CrossRef]
129. Stephanov, M.; Yin, Y. Hydrodynamics with parametric slowing down and fluctuations near the critical point. *Phys. Rev. D* **2018**, *98*, 036006. [CrossRef]
130. Rajagopal, K.; Ridgway, G.; Weller, R.; Yin, Y. Hydro+ in Action: Understanding the Out-of-Equilibrium Dynamics Near a Critical Point in the QCD Phase Diagram. *arXiv* **2019**, arXiv:1908.08539.
131. An, X.; Basar, G.; Stephanov, M.; Yee, H.U. Fluctuation dynamics in a relativistic fluid with a critical point. *arXiv* **2019**, arXiv:1912.13456.
132. Mohanty, B. (National Institute of Science Education and Research, Odisha, India). Private Communications, 2019.
133. Bzdak, A.; Koch, V.; Oliinychenko, D.; Steinheimer, J. Large proton cumulants from the superposition of ordinary multiplicity distributions. *Phys. Rev. C* **2018**, *98*, 054901. [CrossRef]
134. Aggarwal, M.M.; Ahammed, Z.; Alakhverdyants, A.; Alekseev, I.; Alford, J.; Anderson, B.; Arkhipkin, D.; Averichev, G.; Balewski, J.; Barnby, L.; et al. Higher Moments of Net-proton Multiplicity Distributions at RHIC. *Phys. Rev. Lett.* **2010**, *105*, 022302. [CrossRef]
135. Adamczyk, L.; Adkins, J.; Agakishiev, G.; Aggarwal, M.; Ahammed, Z.; Alekseev, I.; Alford, J.; Anson, C.; Aparin, A.; Arkhipkin, D.; et al. Energy Dependence of Moments of Net-proton Multiplicity Distributions at RHIC. *Phys. Rev. Lett.* **2014**, *112*, 032302. [CrossRef]
136. Luo, X. Energy Dependence of Moments of Net-Proton and Net-Charge Multiplicity Distributions at STAR. *PoS CPOD* **2015**, *2014*, 19. [CrossRef]
137. Adam, J.; Adamczyk, L.; Adams, J.; Adkins, J.; Agakishiev, G.; Aggarwal, M.; Ahammed, Z.; Alekseev, I.; Anderson, D.; Aoyama, R. et al. Collision-energy dependence of second-order off-diagonal and diagonal cumulants of net-charge, net-proton, and net-kaon multiplicity distributions in Au + Au collisions. *Phys. Rev. C* **2019**, *100*, 014902. [CrossRef]
138. Luo, X. Exploring the QCD Phase Structure with Beam Energy Scan in Heavy-ion Collisions. *Nucl. Phys. A* **2016**, *956*, 75. [CrossRef]
139. Adam, J.; Adamczyk, L.; Adams, J.; Adkins, J.; Agakishiev, G.; Aggarwal, M.; Ahammed, Z.; Alekseev, I.; Anderson, D.; Aparin, A.; et al. Net-proton number fluctuations and the Quantum Chromodynamics critical point. *arXiv* **2020**, arXiv:2001.02852.
140. Adamczyk, L.; Adkins, J.; Agakishiev, G.; Aggarwal, M.; Ahammed, Z.; Alekseev, I.; Alford, J.; Anson, C.; Aparin, A.; Arkhipkin, D.; et al. Beam energy dependence of moments of the net-charge multiplicity distributions in Au+Au collisions at RHIC. *Phys. Rev. Lett.* **2014**, *113*, 092301. [CrossRef] [PubMed]
141. Adamczyk, L.; Adam, J.; Adamczyk, L.; Adams, J.; Adkins, J.; Agakishiev, G.; Aggarwal, M.; Ahammed, Z.; Ajitanand, N.;Alekseev, I.; et al. Collision Energy Dependence of Moments of Net-Kaon Multiplicity Distributions at RHIC. *Phys. Lett. B* **2018**, *785*, 551. [CrossRef]
142. Aggarwal, M.M.; Ahammed, Z.; Alakhverdyants, A.; Alekseev, I.; Alford, J.; Anderson, B.; Arkhipkin, D.; Averichev, G.; Balewski, J.; Barnby, L.; et al. An Experimental Exploration of the QCD Phase Diagram: The Search for the Critical Point and the Onset of De-confinement. *arXiv* **2010**, arXiv:1007.2613.
143. Luo, X.; Xu, J.; Mohanty, B.; Xu, N. Volume fluctuation and auto-correlation effects in the moment analysis of net-proton multiplicity distributions in heavy-ion collisions. *J. Phys. G* **2013**, *40*, 105104. [CrossRef]
144. Chatterjee, A.; Zhang, Y.; Zeng, J.; Sahoo, N.R.; Luo, X. Centrality selection effect on higher order cumulants of net-proton multiplicity distributions in relativistic heavy-ion collisions. *Phys. Rev. C* **2020**, *101*, 034902. [CrossRef]
145. Bzdak, A.; Koch, V. Local Efficiency Corrections to Higher Order Cumulants. *Phys. Rev. C* **2015**, *91*, 027901. [CrossRef]
146. Luo, X. Unified description of efficiency correction and error estimation for moments of conserved quantities in heavy-ion collisions. *Phys. Rev. C* **2015**, *91*, 034907, Erratum: [Phys. Rev. C **2016**, *94*, 059901] [CrossRef]
147. Kitazawa, M. Efficient formulas for efficiency correction of cumulants. *Phys. Rev. C* **2016**, *93*, 044911. [CrossRef]

148. Nonaka, T.; Kitazawa, M.; Esumi, S. More efficient formulas for efficiency correction of cumulants and effect of using averaged efficiency. *Phys. Rev. C* **2017**, *95*, 064912. [CrossRef]
149. Luo, X.; Nonaka, T. Efficiency correction for cumulants of multiplicity distributions based on track-by-track efficiency. *Phys. Rev. C* **2019**, *99*, 044917. [CrossRef]
150. Luo, X. Error Estimation for Moments Analysis in Heavy Ion Collision Experiment. *J. Phys. G* **2012**, *39*, 025008. [CrossRef]
151. Thäder, J. Higher Moments of Net-Particle Multiplicity Distributions. *Nucl. Phys. A* **2016**, *956*, 320. [CrossRef]
152. Xu, J.; Yu, S.; Liu, F.; Luo, X. Cumulants of net-proton, net-kaon, and net-charge multiplicity distributions in Au + Au collisions at $\sqrt{s_{NN}}$ = 7.7, 11.5, 19.6, 27, 39, 62.4, and 200 GeV within the UrQMD model. *Phys. Rev. C* **2016**, *94*, 024901. [CrossRef]
153. Zhou, C.; Xu, J.; Luo, X.; Liu, F. Cumulants of event-by-event net-strangeness distributions in Au+Au collisions at $\sqrt{s_{\rm NN}}$ = 7.7–200 GeV from UrQMD model. *Phys. Rev. C* **2017**, *96*, 014909. [CrossRef]
154. Bzdak, A.; Koch, V.; Skokov, V. Baryon number conservation and the cumulants of the net proton distribution. *Phys. Rev. C* **2013**, *87*, 014901. [CrossRef]
155. Braun-Munzinger, P.; Rustamov, A.; Stachel, J. Bridging the gap between event-by-event fluctuation measurements and theory predictions in relativistic nuclear collisions. *Nucl. Phys. A* **2017**, *960*, 114. [CrossRef]
156. He, S.; Luo, X.; Nara, Y.; Esumi, S.; Xu, N. Effects of Nuclear Potential on the Cumulants of Net-Proton and Net-Baryon Multiplicity Distributions in Au+Au Collisions at $\sqrt{s_{\rm NN}} = 5$ GeV. *Phys. Lett. B* **2016**, *762*, 296. [CrossRef]
157. He, S.; Luo, X. Proton Cumulants and Correlation Functions in Au + Au Collisions at $\sqrt{s_{\rm NN}}$ = 7.7–200 GeV from UrQMD Model. *Phys. Lett. B* **2017**, *774*, 623. [CrossRef]
158. Zhang, Y.; He, S.; Liu, H.; Yang, Z.; Luo, X. Effects of resonance weak decays and hadronic re-scattering on the proton number fluctuations in Au + Au collisions at $\sqrt{s_{\rm NN}} = 5$ GeV from JAM model. *Phys. Rev. C* **2020**, *101*, 034909. [CrossRef]
159. Adare, A.; Afanasiev, S.; Aidala, C.; Ajitanand, N.; Akiba, Y.; Akimoto, R.; Al-Bataineh, H.; Alexander, J.; Al-Ta'ani, H.; Angerami, A.; et al. Measurement of higher cumulants of net-charge multiplicity distributions in Au+Au collisions at $\sqrt{s_{NN}}$ = 7.7–200 GeV. *Phys. Rev. C* **2016**, *93*, 011901. [CrossRef]
160. Adamczewski-Musch, J.; Arnold, O.; Behnke, C.; Belounnas, A.; Belyaev, A.; Berger-Chen, J.; Biernat, J.; Blanco, A.; Blume, C.; Bohmer, M.; et al. Proton number fluctuations in $\sqrt{s_{NN}}$ = 2.4 GeV Au+Au collisions studies with HADES. *arXiv* **2020**, arXiv:2002.08701.
161. STAR Note 0598: BES-II. white paper. Available online: http://drupal.star.bnl.gov/STAR/starnotes/public/sn0598 (accessed on 28 February 2020).
162. Ablyazimov, T.; Abuhoza, A.; Adak, R.; Adamczyk, M.; Agarwal, K.; Aggarwal, M.; Ahammed, Z.; Ahmad, F.; Ahmad, N.; Ahmad, S.; et al. Challenges in QCD matter physics –The scientific programme of the Compressed Baryonic Matter experiment at FAIR. *Eur. Phys. J. A* **2017**, *53*, 60. [CrossRef]
163. NICA white paper. Available online: http://nica.jinr.ru/files/WhitePaper.pdf (accessed on 28 February 2020).
164. Sun, K.J.; Chen, L.W.; Ko, C.M.; Pu, J.; Xu, Z. Light nuclei production as a probe of the QCD phase diagram. *Phys. Lett. B* **2018**, *781*, 499. [CrossRef]
165. Yu, N.; Zhang, D.; Luo, X. Search for the QCD Critical Point by Transverse Velocity Dependence of Anti-deuteron to Deuteron Ratio. *Chin. Phys. C* **2020**, *44*, 014002. [CrossRef]
166. Liu, H.; Zhang, D.; He, S.; Yu, N.; Luo, X. Light Nuclei Production in Au+Au Collisions at $\sqrt{s_{\rm NN}}$ = 5–200 GeV from JAM model. *arXiv* **2019**, arXiv:1909.09304.
167. Zhang, D. Energy Dependence of Light Nuclei (d, t) Production at STAR. *arXiv* **2019**, arXiv:1909.07028.
168. Zhang, D. Light Nuclei (d, t) Production in Au + Au Collisions at $\sqrt{s_{NN}}$ = 7.7–200 GeV. *arXiv* **2020**, arXiv:2002.10677.
169. Eidelman, S.; Hayes, K.G.; Olive, K.E.; Aguilar-Benitez, M.; Amsler, C.; Asner, D.; Babu, K.S.; Barnett, R.M.; Beringer, J.; Burchat, P.R.; et al. Review of Particle Physics. *Phys. Lett. B* **2004**, *592*, 1. [CrossRef]
170. Zhu, X.; Bleicher, M.; Huang, S.; Schweda, K.; Stocker, H.; Xu, N.; Zhuang, P. $D\bar{D}$ correlations as a sensitive probe for thermalization in high energy nuclear collisions. *Phys. Lett. B* **2007**, *647*, 366. [CrossRef]
171. Cacciari, M.; Nason, P.; Vogt, R. QCD predictions for charm and bottom production at RHIC. *Phys. Rev. Lett.* **2005**, *95*, 122001. [CrossRef] [PubMed]
172. Vogt, R. The Total charm cross-section. *Eur. Phys. J. ST* **2008**, *155*, 213–222. [CrossRef]

173. Abelev, B.; Abrahantes, A.; Adamova, D.; Adare, A.; Aggarwal, M.; Aglieri, G.; Agocs, A.; Agostinelli, A.; Aguilar, S.; Ahammed, Z.; et al. Measurement of charm production at central rapidity in proton-proton collisions at $\sqrt{s}$ = 7 TeV. *JHEP* **2012**, *2012*, 128. [CrossRef]
174. Acosta, D.; Affolder, T.; Ahn, M.; Akimoto, T.; Albrow, M.; Ambrose, D.; Amidei, D.; Anastassov, A.; Anikeev, K.; Annovi, A.; et al. Measurement of prompt charm meson production cross sections in $p\bar{p}$ collisions at $\sqrt{s}$ = 1.96 TeV. *Phys. Rev. Lett.* **2003**, *91*, 241804. [CrossRef]
175. Adamczyk, L.; Agakishiev, G.; Aggarwal, M.; Ahammed, Z.; Alakhverdyants, A.; Alekseev, I.; Alford, J.; Anderson, B.; Anson, C.; Arkhipkin, D.; et al. Measurements of D_0 and D_* production in $p + p$ collisions at $\sqrt{s}$ = 200 GeV. *Phys. Rev. D* **2011**, *86*, 072013. [CrossRef]
176. Ye, Z. Open charm hadron production in $p + p$, Au + Au and U + U collisions at STAR. *Nucl. Phys. A* **2014**, *931*, 520–524. [CrossRef]
177. Adamczyk, L.; Adam, J.; Adamczyk, L.; Adams, J.; Adkins, J.; Agakishiev, G.; Aggarwal, M.; Ahammed, Z.; Ajitanand, N.;Alekseev, I.; et al. Observation of D_0 meson nuclear modifications in Au+Au collisions at $\sqrt{s_{NN}}$ = 200 GeV. *Phys. Rev. Lett.* **2018**, *121*, 229901. [CrossRef]
178. Greco, V.; Ko, C.; Rapp, R. Quark coalescence for charmed mesons in ultrarelativistic heavy-ion collisions. *Phys. Lett. B* **2004**, *595*, 202. [CrossRef]
179. Oh, Y.; Ko, C.; Lee, S.; Yasui, S. Heavy baryon/meson ratios in relativistic heavy-ion collisions. *Phys. Rev. C* **2009**, *79*, 044905. [CrossRef]
180. Zhao, J.; Shi, S.; Xu, N.; Zhuang, P. Sequential coalescence with charm conservation in high energy nuclear collisions. *arXiv* **2018**, arXiv:1805.10858.
181. Plumari, S.; Minissale, V.; Das, S.K.; Coci, G.; Greco, V. Charmed hadrons from coalescence plus fragmentation in relativistic nucleus-nucleus collisions at RHIC and LHC. *Eur. Phys. J. C*, **2018**, *78*, 348. [CrossRef]
182. He, M.; Fries, R.J.; Rapp, R. D_s-meson as quantitative probe of diffusion and hadronization in nuclear collisions. *Phys. Rev. Lett.* **2013**, *110*, 112301. [CrossRef] [PubMed]
183. Agakishiev, G.; Aggarwal, M.; Ahammed, Z.; Alakhverdyants, A.; Alekseev, L.; Alford, J.; Anderson, B.; Anson, C.; Arkhipkin, D.; Averichev, G.; et al. Strangeness enhancement in Cu+Cu and Au+Au collisions at $\sqrt{s_{NN}}$ = 200 GeV. *Phys. Rev. Lett.* **2012**, *108*, 072301. [CrossRef] [PubMed]
184. Abelev, B.; Aggarwal, M.; Ahammed, Z.; Anderson, B.; Arkhipkin, D.; Averichev, G.; Bai, Y.; Balewski, J.; Barannikova, O.; Barnby, L.; et al. Identified baryon and meson distributions at large transverse momenta from Au+Au collisions at $\sqrt{s_{NN}}$ = 200 GeV. *Phys. Rev. Lett.* **2006**, *97*, 152301. [CrossRef] [PubMed]
185. Skands, P.; Carrazza, S.; Rojo, J. Tuning PYTHIA 8.1: The Monash 2013 Tune. *Eur. Phys. J. C* **2014**, *74*, 3024. [CrossRef]
186. Bierlich, C.; Christiansen, J.R. Effects of color reconnection on hadron flavor observables. *Phys. Rev. D* **2015**, *92*, 094010. [CrossRef]
187. Wheaton, S.; Cleymans, J.; Hauer, M. THERMUS: A Thermal model package for ROOT. *Comput. Phys. Commun.* **2009**, *180*, 84. [CrossRef]
188. Adcox, K.; Adler, S.; Ajitanand, N.; Akiba, Y.; Alexander, J.; Aphecetche, L.; Arai, Y.; Aronson, S.; Averbeck, R.; Awes, T.; et al. Measurement of single electrons and implications for charm production in Au+Au collisions at $\sqrt{s_{NN}}$ = 130 GeV. *Phys. Rev. Lett.* **2002**, *88*, 192303. [CrossRef]
189. Frixione, S.; Mangano, M.L.; Nason, P.; Ridolfi, G. Heavy quark production. *Adv. Ser. Direct. High Energy Phys.* **1998**, *15*, 609–706.
190. Adamczyk, L.; Adkins, J.; Agakishiev, G.; Aggarwal, M.; Ahammed, Z.; Ajitanand, N.; Alekseev, I.; Anderson, D.; Aoyama, R.; Aparin, A.; et al. Elliptic flow of electrons from heavy-flavor hadron decays in Au + Au collisions at $\sqrt{s_{NN}}$ = 200, 62.4, and 39 GeV. *Phys. Rev. C* **2017**, *95*, 034907. [CrossRef]
191. Si, F.; Chen, X.; Zhou, L.; Zhang, Y.; Zhang, S.; Ju, X.; Li, X.; Dong, X.; Xu, N. Charm and beauty isolation from heavy flavor decay electrons in Au+Au collisions at $\sqrt{s_{NN}}$ = 200 GeV at RHIC. *arXiv* **2019**, arXiv:1906.08974.
192. Xie, G. Measurements of open charm hadron production in Au+Au Collisions at $\sqrt{s_{NN}}$ = 200 GeV at STAR. *PoS HardProbes2018* **2018**, 142.
193. Sjöstrand, T.; Mrenna, S.; Skands, P. PYTHIA 6.4 Physics and Manual. *JHEP* **2006**, *605*, 26. [CrossRef]
194. Tavernier, S.P.K. Charmed and bottom flavored particle production in hadronic interactions. *Rep. Prog. Phys.* **1987**, *50*, 1439–1489. [CrossRef]
195. Bamberger, A.; Binon, F.; Bricman, C.; Bruning, H.; Duteil, P.; Gouanere, M.; Hartung, R.; Jansen, J.; Lagnaux, J.; Massas, G.; et al. J/psi production by 24 GeV/c protons. *Nucl. Phys. B* **1978**, *134*, 1. [CrossRef]

196. Corden, M.J.; Dowell, J.; Garvey, J.; Homer, R.; Jobes, M.; Kenyon, I.; McMahon, T.; Owen, R.; Sumorok, K.; Vallance, R.; et al. Experimental results on J/ψ production by $\pi^{\pm}$, $K^{\pm}$, p and $\bar{p}$ incident on hydrogen at 39.5 GeV/c. *Phys. Lett. B* **1981**, *98*, 220. [CrossRef]
197. Antipov, Y.M.; Bessubov, V.; Budanov, N.; Bushnin, Y.; Denisov, S.; Gorin, Y.; Lebedev, A.; Lednev, A.; Mikhailov, Y.; Petrukhin, A.; et al. J/ψ particle production by 70 GeV/c protons. *Phys. Lett. B* **1976**, *60*, 309. [CrossRef]
198. Snyder, H.D.; Hom, D.; Lederman, L.; Paar, H.; Weiss, J.; Yoh, J.; Appel, J.; Brown, B.; Brown, C.; Innes, W.; et al. Production of Υ(3100) and Ψ'(3700) in p-Be collisions at 400 GeV. *Phys. Rev. Lett.* **1976**, *36*, 1415. [CrossRef]
199. Anderson, K.J.; Henry, G.; McDonald, K.; Pilcher, J.; Rosenberg, E.; Branson, J.; Sanders, G.; Smith, A.; Thaler, J. Production of muon pairs by 150 GeV/c π^+ and protons. *Phys. Rev. Lett.* **1976**, *36*, 237. [CrossRef]
200. Anderson, K.J.; Coleman, B.; Hogan, G.; Karhi, H.; McDonald, K.; Newman, C.; Pilcher, J.; Rosenberg, E.; Sanders, G.; Smith, A.; et al. Production of muon pairs by 225 GeV $\pi^{\pm}$, $K^{\pm}$, $p^{\pm}$ beams on nuclear targets. *Phys. Rev. Lett.* **1979**, *42*, 944. [CrossRef]
201. Siskind, E.J.; Barish, B.; Bartlett, J.; Bodek, A.; Merritt, F.; Shaevitz, M.; Diamant-Berger, A.; Dishaw, J.; Faessler, M.; Liu, J.; et al. Production of Υ(3100) in 400 GeV/c proton interactions. *Phys. Rev. D* **1980**, *21*, 628. [CrossRef]
202. Gribushin, A.; Abramov, V.; Antipov, Y.; Baldin, B.; Crittenden, R.; Davis, C.; Dauwe, L.; Denisov, S.; Dyshkant, A.; Dzierba, A.; et al. Production of J/ψ mesons in p-Be collisions at 530 GeV/c and 800 GeV/c. *Phys. Rev. D* **2000**, *62*, 012001. [CrossRef]
203. Antoniazzi, L.; Arenton, M.; Cao, Z.; Chen, T.; Conetti, S.; Cox, B.; Delchamps, S.; Fortney, L.; Guffey, K.; Haire, M.; et al. A measurement of J/ψ and ψ' production in 300 GeV/c proton, anti-proton and $\pi^{\pm}$ nucleon interactions. *Phys. Rev. D* **1992**, *46*, 4828. [CrossRef]
204. Alexopoulos, T.; Antoniazzi, L.; Arenton, M.; Ballagh, H.; Bingham, H.; Blankman, A.; Block, M.; Boden, A.; Bonomi, G.; Cao, Z.; et al. Differential cross-sections of J/ψ and ψ' in 800 GeV/c p-Si interactions. *Phys. Rev. D* **1997**, *55*, 3927. [CrossRef]
205. Schub, M.H.; Jansen, D.; Mishra, C.; Ho, P.; Brown, C.; Carey, T.; Chen, Y.; Childers, R.; Cooper, W.; Darden, C.; et al. Measurement of J/ψ and ψ' production in 800 GeV/c proton-gold collisions. *Phys. Rev. D* **1995**, *52*, 1307. [CrossRef]
206. Badier, J.; Boucrot, J.; Bourotte, J.; Burgun, G.; Callot, O.; Charpentier, P.; Crozon, M.; Decamp, D.; Delpierre, P.; Gandois, B.; et al. Experimental J/ψ hadronic production from 150 GeV/c to 280 GeV/c. *Z. Phys. C* **1983**, *20*, 101.
207. Abreu, M.C.; Baglin, C.; Baldit, A.; Bedjidian, M.; Bordalo, P.; Bussiere, A.; Busson, P.; Castor, J.; Chambon, T.; Charlot, C.; et al. Charmonia production in 450 GeV/c proton induced reactions. *Phys. Lett. B* **1998**, *444*, 516. [CrossRef]
208. Alessandro, B.; Alexa, C.; Arnaldi, R.; Atayan, M.; Baglin, C.; Baldit, A.; Beole, S.; Boldea, V.; Bordalo, P.; Borenstein, S.; et al. Charmonium production and nuclear absorption in p-A interactions at 450 GeV. *Eur. Phys. J. C* **2004**, *33*, 31.
209. Abreu, M.C.; Alessandro, B.; Baldit, A.; Barriere, C.; Bedjidian, M.; Bordalo, P.; Castor, J.; Chambon, T.; Chaurand, B.; Chiavassa, E.; et al. J/ψ and ψ' and Drell-Yan production in pp and pd interactions at 450 GeV/c. *Phys. Lett. B* **1998**, *438*, 35. [CrossRef]
210. Morel, C.; Bernasconi, A.; Breedon, R.; Camilleri, L.; Cool, R.; Cox, P.; Cushman, P.; Dick, L.; Dukes, E.; Gabioud, B.; et al. Measurement of the inclusive J/ψ production cross-sections in $\bar{p}p$ and pp collisions at $\sqrt{s}$ = 24.3 GeV. *Phys. Lett. B* **1990**, *252*, 505. [CrossRef]
211. Abt, I.; Adams, M.; Agari, M.; Albrecht, H.; Aleksandrov, A.; Amaral, V.; Amorim, A.; Aplin, S.; Aushev, V.; Bagaturia, Y.; et al. Measurement of the J/ψ production cross section in 920 GeV/c fixed-target proton-nucleus interactions. *Phys. Lett. B* **2006**, *638*, 407. [CrossRef]
212. Nagy, E.; Regler, M.; Schmidt-Parzefall, W.; Schubert, K.; Winter, K.; Brandt, A.; Dibon, H.; Flugge, G.; Niebergall, F.; Schumacher, P.; et al. Observation of high mass μ^+ μ^- pairs at the ISR. *Phys. Lett. B* **1975**, *60*, 96. [CrossRef]
213. Adler, S.S.; Afanasiev, S.; Aidala, C.; Ajitanand, N.; Akiba, Y.; Alexander, J.; Amirikas, R.; Aphecetche, L.; Aronson, S.; Averbeck, R.; et al. J/ψ production from proton proton collisions at $\sqrt{s}$ = 200 GeV. *Phys. Rev. Lett.* **2004**, *92*, 051802. [CrossRef]

214. Maltoni, F.; Spengler, J.; Bargiotti, M.; Bertin, A.; Bruschi, M.; Castro, S.; Fabbri, L.; Faccioli, P.; Giacobbe, B.; Grimaldi, F.; et al. Analysis of charmonium production at fixed-target experiments in the NRQCD approach. *Phys. Lett. B* **2006**, *638*, 202–208. [CrossRef]
215. Vogt, R. Phenomenology of charm and bottom production. *Z. Phys. C* **1996**, *71*, 475–481. [CrossRef]
216. Nonaka, T. Measurement of the Sixth-Order Cumulant of Net-Particle Distributions in Au+Au Collisions from the STAR Experiment. In Proceedings of the QM2019, Wuhan, China, 4–9 November 2019.
217. Pandav, A. Measurement of cumulants of conserved charge multiplicity distributions in Au+Au collisions from the STAR experiment. In Proceedings of the QM2019, 4–9 November 2019, Wuhan, China.
218. Geraksiev, N.S. The Nuclotron-based Ion Collider Facility Project. The Physics Programme for the Multi-Purpose Detector. *J. Phys. Conf. Ser.* **2019**, *1390*, 012121. [CrossRef]
219. Cassing, W.; Bratkovskaya, E.; Sibirtsev, A. Open charm production in relativistic nucleus-nucleus collisions. *Nucl. Phys. A* **2001**, *691* 753. [CrossRef]
220. Available online: https://www.gsi.de/work/forschung/cbmnqm/cbm.htm (accessed on 28 February 2020).
221. STAR Endcap TOF Proposal. Available online: https://drupal.star.bnl.gov/STAR/starnotes/public/sn0665 (accessed on 28 February 2020).
222. STAR iTPC upgrade Proposal. Available online: https://drupal.star.bnl.gov/STAR/starnotes/public/sn0644 (accessed on 28 February 2020).